First Alps-wide reconstruction of LGM glacial sediment transport enabled by GPU-accelerated particle tracking

Tancrède P. M. Leger[1], Guillaume Jouvet[1], Sarah Kamleitner[1,2], Brandon D. Finley[1], Maxime Bernard[1], Balthazar Allegri[1], Frédéric Herman[1], Andreas Vieli[2], Andreas Henz[2], Samuel U. Nussbaumer[2]

[1]Institute of Earth Surface Dynamics, University of Lausanne, Lausanne, Switzerland
[2]Department of Geography, University of Zürich, Zürich, Switzerland

Correspondence: Tancrède P. M. Leger (tancrede.leger@unil.ch): personal address: tankleger@gmail.com

Abstract. Reconstructing the transport histories and provenances of glacial sediments and ice-contact deposits (e.g. tills, moraines) in formerly glaciated regions remains a major challenge, particularly at icefield-to ice-sheet scales and over multi-millennial timescales. Yet such reconstructions are central to key questions in Quaternary science, including estimates of past glacial erosion rates and sediment fluxes, the role of subglacial sediment storage in erosion reduction, or the reconstruction of past ice-flow dynamics, ice divides, and transfluences. While numerical modelling can enable one to reproduce past glacial sediment transport via coupling glacier models with particle tracking, this becomes computationally unfeasible over large spatial domains and paleo timescales using traditional computing. As a result, no study to date has simulated glacial sediment transport using large particle numbers (tens of millions) across continental-scale icefields such as the one occupying the European Alps during the Last Glacial Maximum (LGM). Here, we overcome this limitation using the Instructed Glacier Model (IGM), which allows the coupling of 3D Lagrangian particle tracking with high-resolution glacier simulations, both accelerated on Graphics Processing Units (GPU). This unlocks the modelling of ice advection of millions of particles at minimal additional computational cost, allowing simulations of glacial sediment transport across the European Alps over multi-millennial timescales (40-18 ka) and at the unprecedented spatial resolution of 300 m. We achieve ~50x faster computation tracking 20 million particles across the Alps using a single GPU instead of 60 CPU threads. In doing so, we produce the first Alps-wide modelling reconstruction of glacial sediment transport during the LGM, using process-based particle seeding schemes to represent both subglacial (e.g. abrasion, plucking) and supraglacial (e.g. rockfall, landslides) sediment sourcing. Results are analysed through complementary ‘sink-to-source’ (deposit provenance) and ‘source-to-sink’ (potential depositional pathways) analyses, enabling us to reconstruct the LGM glacial transport of numerous ice-contact deposits and surface lithologies across the Alps. We find that supraglacially sourced glacial sediments are typically eroded earlier, experience longer glacier residence times, and undergo greater cumulative ice-free exposure than those of subglacial origin, with implications for the interpretation of cosmogenic nuclide inheritance in glacial deposits. Our new coupled glacier-particle modelling framework opens avenues for quantitative model-data comparisons using glacial geomorphology and provides a powerful tool for reconstructing paleo ice dynamics, sediment provenance, and Quaternary glacial landscape evolution.

1 Introduction

In the early 1800s, pioneering naturalists argued certain sediments found in mountain forelands evidenced widespread past glacier expansions, an idea commonly known as the ‘glacier theory’ (e.g. Esmark, 1824; Venetz, 1830; Agassiz, 1840; Lyell, 1840). Their hypotheses were later validated by investigations characterizing deposits emplaced at the lateral, frontal, or subglacial margins of former glaciers, icefields, and ice sheets (Sugden & John, 1976). These so-called ‘ice-contact deposits’ include erratic boulders, lateral and terminal moraines, till units, drumlins, eskers, lineations, and various other glacio-depositional landforms (Evans & Benn, 2004). Over the last two centuries, glacial geologists have studied these features across formerly glaciated landscapes to reconstruct the extent, duration, style, and timing of past glacier advances and retreats (e.g. Penck & Brückner, 1909; Evans et al., 2006; Ehlers et al., 2011; Davies et al., 2012; Clark et al., 2022). In the European Alps, a long tradition of such work has focused on reconstructing Quaternary glaciations of the former Alpine Ice Field (AIF) (e.g. Geikie, 1910; van Husen, 1997; Kelly et al., 2004; Preusser et al., 2010, 2011; Graf et al., 2015; Ivy-Ochs, 2015; 2022). Consequently, the processes of ice-contact sediment deposition and post-depositional disturbance are often well documented in many regions.

By contrast, the pre-depositional histories of ice-contact deposits are often poorly constrained. The inaccessibility and complexity of glacial sediment erosion/transport processes challenge empirical characterization in modern glacier systems, and even more so in paleo settings (Boulton, 1996). Field studies attempting to quantify pre-depositional histories in active glacier systems use techniques such as mineralogical provenance analyses (e.g. Herman et al., 2015), detrital and *in situ* low-temperature thermochronology (e.g. Enkelmann & Ehlers, 2015), terrestrial cosmogenic nuclide concentrations (e.g. Guillon et al., 2015), morainic soil material’s fingerprinting analysis (e.g. Mohammadi et al., 2024), or luminescence rock surface burial dating (Margirier et al., 2025). However, such studies are rare, often limited to individual deposits or catchments, and difficult to extend to paleo glacier events. As a result, the provenance, erosion histories, transport distances, durations, and pathways of ice-contact deposits remain highly challenging to constrain at larger spatial and longer temporal scales.

Understanding glacial sediment erosion/transport history and their provenance is critical for multiple research questions. Such insights can, for instance, improve estimates of Quaternary glacial erosion rates and sediment fluxes, complementing studies of glaciofluvial sediment export dynamics (e.g. Koppes et al., 2015; Herman et al., 2015; Lane et al., 2017; Overeem et al., 2017; Delaney et al., 2023). They also inform mechanisms and timescales of debris cover and subglacial sediment storage, which can for instance be involved in protecting bedrock from subglacial erosion (Delaney & Anderson, 2022). Pre-depositional sediment histories can also reveal past ice dynamics, including interactions with topography and the mechanisms of flow convergence/divergence associated with tributary glaciers merging or separating during waxing and waning cycles of ice sheets or icefields (Jouvet et al., 2017). These reconstructions aid in identifying former ice-flow regimes and the position or migration of ice divides, key to interpreting sedimentary archives of past ice-flow directionality (e.g. Hughes et al., 2010; Kamleitner et al., 2024) and to mapping former ice transfluences (e.g. Reitner et al., 2010). Moreover, knowing whether a deposit reached glacier ice supraglacially or subglacially, and its glacial transport history, supports the application of geochronological methods (e.g. cosmogenic exposure or luminescence dating), where prior exposure to sunlight or the atmosphere can affect age interpretations (e.g. Heyman et al., 2011). Quantifying glacial sediment routing and export in formerly glaciated landscapes is also crucial to inform industries such as concerned with aggregate resources or the geological disposal of nuclear waste (e.g. Fischer et al., 2015; 2021). Indeed, quantifying past long-term glacial sediment export and deposition dynamics helps better project future geological stability and future glaciations' impacts on possible industrial repository sites via basal erosion, ensuring safe containment of anthropogenic waste over millennia. Lastly, tracking the transport history of iconic glacial erratics, some of which have cultural significance (Reynard, 2004; Coutterand, 2018), offers an opportunity to bridge scientific understanding with public engagement. The permanent glacial erratics exhibition of Grenchen (Solothurn, Switzerland) displaying erratics found during construction works, is a prime example of a cultural connection to the paleo-glacial heritage. Thus, while it represents a substantial challenge, characterizing the pre-depositional history of glacial sediments and ice-contact deposits yields widespread implications for numerous research fields and industrial/societal activities.

Numerical modelling offers a means to address the above knowledge gaps by generating spatially distributed, time-evolving estimates of glacial sediment transport which can be compared against empirical data such as glacial erratic mapping and ice-contact sediment provenance analyses (e.g. Veness et al., 2025). A robust and established method consists in coupling a glacier evolution model with Lagrangian particle tracking to simulate the time-transient advection of sediment-like particles by ice-flow (e.g. Rybak & Huybrechts, 2003; Rowan et al., 2015; Bernard et al., 2020; Scherler & Egholm, 2020). In a Lagrangian approach, numerical operations are performed on individual moving particles themselves rather than at fixed grid locations, allowing to track the particles' paths through the evolving glacier at sub-grid scales. When modelled glacier geometries are somewhat consistent with empirical evidence, and when particle seeding is parameterised to mimic real sediment erosion processes, this method can produce first-order estimates of glacial sediment transport pathways (Margirier et al., 2025). However, no studies have yet tracked large particle numbers ($>10^6$) within model simulations of past Alpine Ice Field (AIF) glaciations. This is largely due to two constraints. First, previous AIF simulations (e.g. Mey et al., 2016; Seguinot et al., 2018; Jouvet et al., 2023) exhibited potent mismatches in ice thickness compared to trimline elevation field data (e.g. Kelly et al., 2004; Hippe et al., 2014), limiting confidence in inferred ice-flow dynamics. Second, standard numerical approaches impose a high computational cost and high memory requirement when conducting Lagrangian tracking of large particle numbers: i.e. tens to hundreds of millions of particles. Given the highly ubiquitous nature of sediments in glacier systems, such high particle numbers are essential if one wants to realistically depict some of the natural processes involved (Rowan et al., 2015). Consequently, no studies to date have simulated glacial sediment transport using large particle numbers across continental-scale icefields like the AIF at any timescale, let alone over thousands of years.

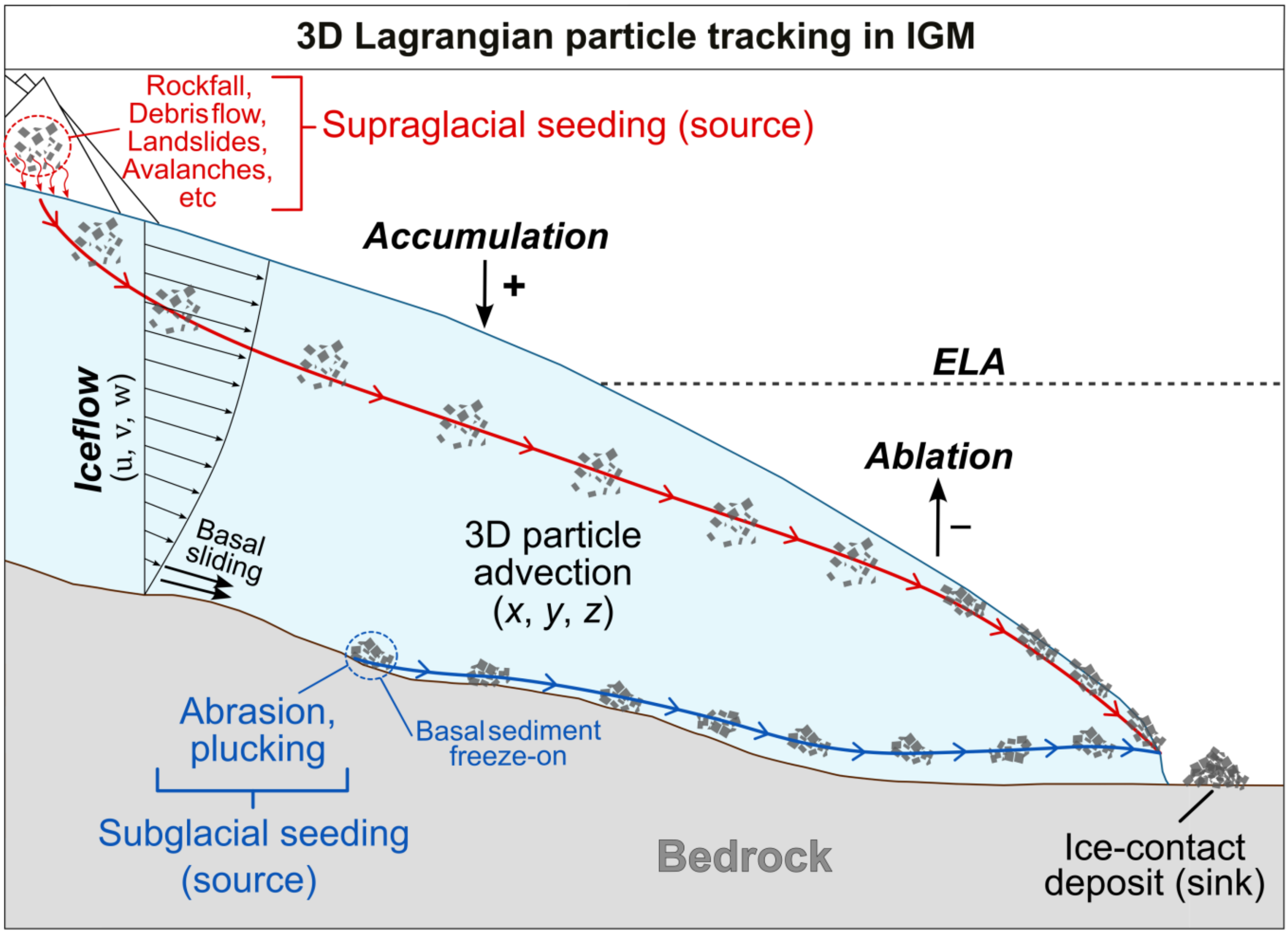

Figure 1. Simplified schematic diagram illustrating the Graphics-Processing-Units (GPU) - based, 3D Lagrangian particle advection scheme of both supraglacially seeded (red) and subglacially seeded (blue) particles coupled with our Instructed Glacier Model (IGM) setup and implemented in this study. 'ELA' stands for 'Equilibrium Line Altitude'.

Here we show that these bottlenecks can be overcome. Leger et al. (2025) produced an ensemble of 100 high-resolution (300 m) simulations of the AIF during the Last Glacial Maximum (LGM), whose best-performing simulations improved model-data agreement in both ice thickness and extent compared to previous efforts (e.g. Seguinot et al., 2018; Jouvet et al., 2023). These advances were enabled by the Instructed Glacier Model (IGM), a high-order, thermo-mechanically coupled glacier evolution model (Jouvet et al., 2021; Jouvet & Cordonnier, 2023). IGM leverages physics-informed machine learning and computation on Graphics Processing Units (GPU) to reduce the computational cost of traditional glacier modelling by several orders of magnitude. Here we show that IGM's novel GPU-based architecture also enables efficient parallelization of Lagrangian particle tracking, enabling the coupling of the advection of millions of particles within our AIF model framework at minimal additional cost (see Results section for quantifications) and consequently track the glacial-transport trajectories of individual particles from their location of origin (the source) to their final deposition site (the sink).

To this end, we conduct a new set of Alps-wide simulations of the last glaciation of the European Alps using the same data-consistent IGM setup as Leger et al. (2025) with the additional coupling of 3D Lagrangian tracking of large particle numbers. Ultimately, we produce the first Alps-wide model estimates of time-transient and 3D glacial sediment trajectories between 40 and 18 ka, the period bracketing the LGM. We design a new particle advection module and seeding scheme that simulates both the subglacial (e.g. via abrasion, plucking) and supraglacial (e.g. via rockfall, debris flow) origins of glacially transported sediments (Fig. 1). This new method allows us to simulate the complex glacial-transport trajectories of LGM ice-contact deposits (e.g. terminal moraines) across the Alps at high spatial (300 m) and temporal (10 yr) resolutions, and estimate their provenances, glacial transport time, erosion timing, and cumulative ice-free time during their source-to-sink journey. With this experiment, we also model the possible LGM source-to-sink trajectories of certain surface lithologies (i.e. sources) throughout the Alps, which we subsequently compare against empirical data on LGM-dated erratics of known location and lithology (e.g. Kamleitner et al., 2022).

2 Methods

2.1 Model setup

IGM is a thermo-mechanical 3D glacier evolution model enhanced with physics-informed deep learning using a convolutional neural network emulator (Jouvet & Cordonnier, 2023) of the high-order 'Blatter-Pattyn' ice-flow solver (Blatter, 1995). In this study, we build on the results of Leger et al. (2025) and use the exact same IGM model version (2.2.1), spatial resolution (300 m), input parameters, and forcings as used for their ensemble's (n=100) best-scoring simulation, i.e. simulation 37 (see Figs. 1, 6 in Leger et al., 2025). We also run our simulations using the same GPU (Nvidia RTX 4090). In Leger et al. (2025), a perturbed-parameter ensemble of 100 simulations was performed, covering 35-18 ka at 300 m spatial resolution across the European Alps, an order-of-magnitude improvement over previous 1-2 km models (Seguinot et al., 2018; Jouvet et al., 2023). Their model setup (and thus also ours) integrates modules for ice-enthalpy (after Aschwanden et al., 2012), surface mass balance (after Calov & Greve, 2005), isostatic adjustment (after Wickert, 2015), and avalanching for mass re-distribution down steep slopes. The climate forcing was produced by Russo et al. (2024) (also used by Jouvet et al., 2023), who conducted regional downscaling over Europe (2 km resolution) of global Earth-system model outputs using the Weather Research and Forecasting model, providing gridded fields of temperature and precipitation for both the LGM (24 ka) and the pre-industrial era (1850 AD). A glacial index scheme generates continuous climate forcing interpolating these two states using independent local proxy climate data that combines pollen and speleothem records (Fig. 2e in Leger et al., 2025; Luetscher et al., 2015; Duprat-Oualid et al., 2017). Basal sliding is parameterized following a nonlinear Weertman friction condition (e.g. Schoof & Hewitt, 2013) with a sliding coefficient also influenced by enthalpy-driven basal meltwater content and elevation-dependent basal materials' strength, following Bueler & van Pelt (2015) and the Mohr-Coulomb law (Cuffey & Paterson, 2010). For the bed topography, as in Leger et al. (2025)'s simulation 37, we use the digital elevation model from Mey et al. (2016) which includes the removal of (1) present-day glacier thicknesses and lake depths, and (2) reconstructed present-day valley-fill sediment thicknesses in main overdeepenings throughout the Alps. More detailed methods and model descriptions are presented in Leger et al. (2025).

Here, we employ this model setup to run two new simulations featuring the additional coupling of 3D Lagrangian particle tracking. The first simulation is parameterised for subglacial particle seeding whilst the second for supraglacial particle seeding (Fig. 1). We run all simulations between 40 and 18 ka, thus starting 5 kyr earlier than the original setup. While Leger et al. (2025) showed that starting the simulation before 35 ka had no noticeable impact on the modelled AIF geometry during the LGM (~24.8 ka in their simulations), preliminary tests showed that it does affect the diversity of modelled particle trajectories (more details in Results section).

2.2 Particle seeding schemes

For each model time step (every 0.01-0.04 yr) and domain cell (n = 6,030,036), we implement a set of conditions to determine whether to 'seed' (i.e. create) a new particle or not. We exclusively focus on estimating glacial sediment trajectories and transport statistics, and do not address the volumes of glacial sediments, erosion, or deposits. Therefore, seeding of a new particle can be interpreted as the creation of a new glacial 'sediment entity' within the glacier system, possibly ranging in size from grains to large boulders. Note that throughout this paper, we use the terms 'glacial sediment' and 'glacial transport' to describe all sediments that are transported by glacier ice, thus combining supraglacial, englacial, and subglacial debris/transport. Below, we describe the set of conditions required for both subglacial seeding and supraglacial seeding to occur in our model (Fig. 2).

The frequency and spatial distribution of subglacial seeding is here set to be a function of basal ice velocity, as frequently observed (Humphrey & Raymond, 1994; Herman et al., 2015; Cook et al., 2020; Herman et al., 2021). Here, we use the subglacial erosion law obtained by Koppes et al. (2015) from results on sediment export volumes from several outlet glaciers of the Patagonian and Antarctic Peninsula icefields. This non-linear erosion law assumes the erosion rate $\dot{e}$ is proportional to the sliding velocity u_s raised to a power, using an erodibility constant $K_g = 5.2\ x10^{-11}$ and a sliding velocity exponent of $l = 2.34$:

$$\dot{e} = K_g |u_s|^l \qquad 1)$$

We follow Seguinot & Delaney (2021) and assume glacier systems studied by Koppes et al. (2015) likely yield similar dynamics to former outlet glaciers of the AIF during the LGM. Using this law, our model computes an erosion rate and cumulative erosion over time for each grid cell (Fig. 2). Computed erosion is not used to modify the bed topography dynamically but rather only as a quantitative proxy for particle seeding. Once this artificial cumulative erosion reaches a certain threshold (here set to 4 cm), seeding occurs and the erosion value is reset to 0, thus adding a new particle to the system (Fig. 2). This value (4 cm) is arbitrary and represents a parameter to control the total number of advected particles. To add stochasticity to the modelled creation and freeze-on of subglacial sediment, seeding further requires meeting a condition of time delay since last seeding occurred. This time delay is set to randomly vary between 10 and 60 yrs during the simulation following a uniform probability distribution (Fig. 2). Thus, even though erosion is positively correlated to basal ice velocity, some randomness is here introduced in whether seeding will occur shortly or with some delay after the cumulative erosion threshold is reached. Note that with this scheme, we do not model the glaciofluvial transport of subglacially eroded materials, as our model setup is not yet coupled to a subglacial hydrological-routing module. Instead, we exclusively focus on subglacially eroded materials which freeze on and are subsequently advected by glacier ice (Alley et al., 1998). The limitations of this assumption are further mentioned in the Discussion section.

For supraglacial seeding, our scheme was conceived to simulate mechanisms generating supraglacial debris on glaciers, i.e. gravitational mass wasting events including rockfall, rock avalanches, debris flow, avalanches, or landslides (Benn et al., 2012). We assume these events require both no (or little) ice cover and steep slopes to occur. We define all slopes steeper than 45° as susceptible to mass wasting (Fig. 2), following recommendations from Fischer et al. (2012). However, our 300 m model resolution still smooths high-elevation peaks and steep slopes resulting in fewer locations >45° steep than in reality. To avoid this bias, we use a higher-resolution digital elevation model (30 m resolution; Tadono et al., 2014) to produce a mask of pixels meeting a >45° slope condition. We consider all modelled ice that is <20 m thick and located in pixels meeting the high-resolution >45° slope mask to be an artifact of our 300 m resolution, thus representing regions that would have no (or negligible) ice cover in reality. As a result, in our setup, a given grid cell needs to both satisfy the >45° slope condition (in the high-resolution mask) and display modelled ice thickness <20 m, for supraglacial seeding to occur (Fig. 2).

As with subglacial seeding (see above), we introduce stochasticity in supraglacial debris production. Firstly, supraglacial seeding only occurs when meeting a Boolean mask condition (True/False array) randomly shuffled for all domain cells (at every time step) with a True-value likelihood of 80%. Following this, seeding also only occurs when meeting a time delay set to randomly vary between 20 and 160 yrs during the simulation (Fig. 2). All random sampling follows a uniform probability distribution. These additional conditions separately add temporal and spatial randomness to supraglacial seeding, thus applying a probabilistic algorithm; common in mass-wasting event modelling (e.g. Champel et al., 2002). Therefore, while gravitational mass wasting events are highly likely where/when the model features steep slopes (>45°) and a lack of ice cover, they are not necessarily going to occur at every time step and always in the same locations (Fig. 2). Once seeded, particles are advected downslope following the steepest descent until slope angle <45°, or until reaching cells with modelled ice, in which case ice advection will take over (Fig. 2).

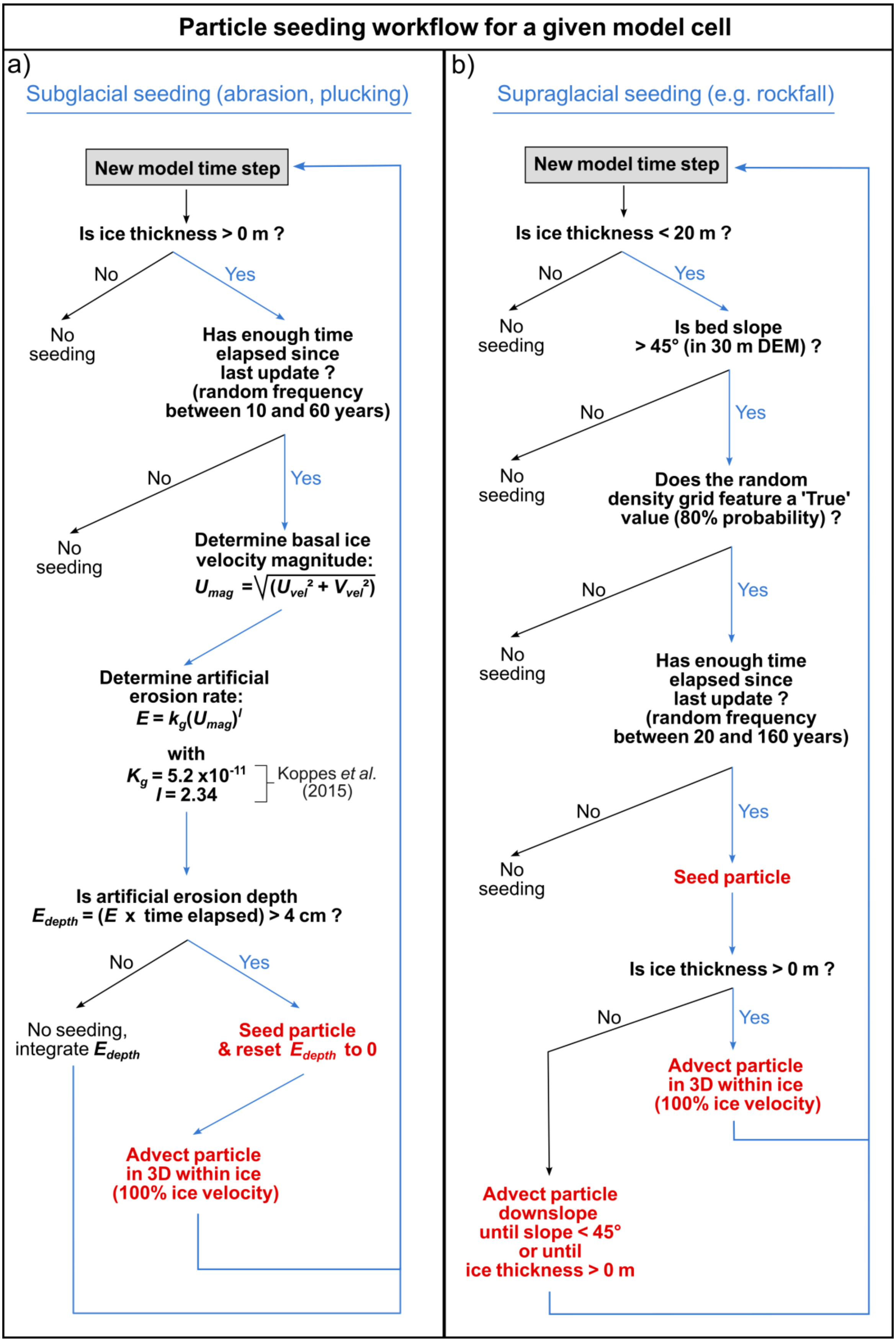

Figure 2. Decision chart indicating the model workflow specific to our particle seeding schemes for a given model cell (n = 6,030,036), and for the two cases of (a) subglacial seeding (abrasion, plucking) and (b) supraglacial seeding (e.g. rockfall, rock avalanche, debris flow, landslides, etc.). This chart summarizes the set of conditions and parameters applied to every model cell and at every model timestep (every 0.01-0.04 yr) during the simulation in order to seed, or not seed, a new particle within the model system.

2.3 Particle Lagrangian advection scheme

To track the movement of particles in 3D within the evolving glacier geometry, we use a fully GPU-optimized Lagrangian advection scheme which computes the space-time trajectory of particles created from seeding and resolves the precise 3D positions of particles at sub-grid resolution. This new scheme builds on the original IGM 'particles' module ((Jouvet et al., 2024) to provide additional computational gains for large-scale particle tracking. At each model timestep, IGM computes the 3D ice-flow based on a high-order stress-balance model referred to as the 'Blatter-Pattyn' model (Blatter, 1995) and thus outputs a 3D velocity field. Each particle's horizontal (x, y) and vertical (z) positions are thus updated according to ice velocity components u, v, w, respectively, integrated over a model timestep, Δt, using an explicit Euler scheme.

$$\begin{aligned} x^{n+1} &= x^n + \Delta t \cdot \bar{u}, \\ y^{n+1} &= y^n + \Delta t \cdot \bar{v}, \\ z^{n+1} &= z^n + \Delta t \cdot \bar{w}, \end{aligned} \quad 2)$$

where $\bar{u}, \bar{v}, \bar{w}$ represent the bilinearly interpolated horizontal and vertical velocities, respectively, at a particle's current location (x^n, y^n). We ensure no particles artificially leave the ice column due to numerical integration errors or transient velocity fluctuations by clipping their relative (normalized) vertical positions to between 0 (bed) and 1 (ice surface). The bilinear interpolation for a scalar field f at a sub-grid location (x, y) is computed using:

$$\bar{f}(x, y) = \sum_{i,j} f_{i,j} \cdot (1 - |x - i|) \cdot (1 - |y - j|) \quad 3)$$

where the summation runs over the four grid nodes surrounding the particle's horizontal position, and the weights $(1 - |x - i|)$ and $(1 - |y - j|)$ ensure a smooth linear interpolation based on the distances to these nodes.

We assume all particles are advected at the velocity of the ice. The limitations of this assumption are assessed in the Discussion section below. When a particle reaches the modelled ice margin and is deposited, i.e. when ice thickness at its position becomes 0 m, it is prescribed the bed elevation. If local slope is <45° this particle will remain stagnant (Fig. 2). If the modelled glacier re-advances and local ice thickness is >0 m again, the particle gets re-entrained and 3D ice advection computations restart. We thus assume that all temporarily deposited sediments freeze-on and get re-entrained by a re-advancing ice margin. Although reality is more complex whereby former deposits can be overridden and survive younger glacier advances, the process of re-entrainment is here considered to dominate (Cogez et al., 2018). This assumption is supported by the general rarity, in formerly glaciated landscapes, of preserved older moraines inboard of younger and more extensive terminal moraines (Gibbons et al., 1984).

Although particle positions are computed at every timestep (0.01-0.04 yr), they are saved every 10 model years, which for our simulated timeframe (40-18 ka) generates 2200 data frames for each of the millions of advected particles (20.5 million at maximum). The data saved for each particle include its x and y coordinates, relative height in ice column, seeding year, and cumulative glacial transport time since seeding. 10 years is the highest output frequency achieved while ensuring the particle database (~1.22 TB) can be post-processed at a manageable computational cost. At that output temporal frequency, the post-processing mapping of particle trajectories fully reflects the simulated ice-flow and particle advection in most cases, except where modelled ice velocities are both high (e.g. >1000 m yr^{-1}) and towards highly sinuous glacier motion (e.g. around valley bends), where mapping particle positions every 10 years can result in unrealistically straight trajectories. This will however only impact the mapped trajectory towards the bend and not reduce the accuracy of its modelled provenance nor destination.

2.4 Reconstructing glacial sediment trajectories

After running the glacier-particle coupled IGM simulations, we use the output database of particle coordinates to map the time-transient trajectories of certain particles. This is conducted within the frame of two analyses. The first one, hereafter referred to as the 'sink-to-source' analysis, aims at reconstructing the provenance and glacial transport pathways of specific LGM terminal ice-contact deposits. The second analysis, called 'source-to-sink', addresses the opposite question. Its objective is to estimate the possible transport pathways and deposition locations of glacial sediments eroded from a pre-determined source.

The sink-to-source analysis involves finding all particles that end up within the area of a mapped deposit at the end of the simulation (18 ka), after final glacier retreat, and trace back their glacial transport trajectories. Although this can be achieved for any user-defined polygon, we focus on ice-contact deposits located towards the terminal margins of main AIF outlet glaciers during the LGM (e.g. LGM moraines). To follow a consistent methodology across the Alps, we map a series of 49 polygons (Fig. 3a) covering the area between our most extensive time-independent modelled ice margin and the empirical LGM outline of the AIF originally produced by Ehlers et al. (2011) and improved by several studies since (Gianotti et al., 2008; 2015; Ravazzi et al., 2012; Monegato et al., 2017; Federici et al., 2017; Ivy-Ochs et al., 2018; Braakhekke et al., 2020; Kamleitner et al., 2022; 2023; Ribolini et al., 2022). Tracing polygons over that area between ensures that we isolate all particles deposited at the LGM margins even where model-data fit in ice extent is not perfect, which is still the case despite improvements relative to former AIF-wide LGM models (Seguinot et al., 2018; Jouvet et al., 2023; see Fig. 4a in Leger et al., 2025).

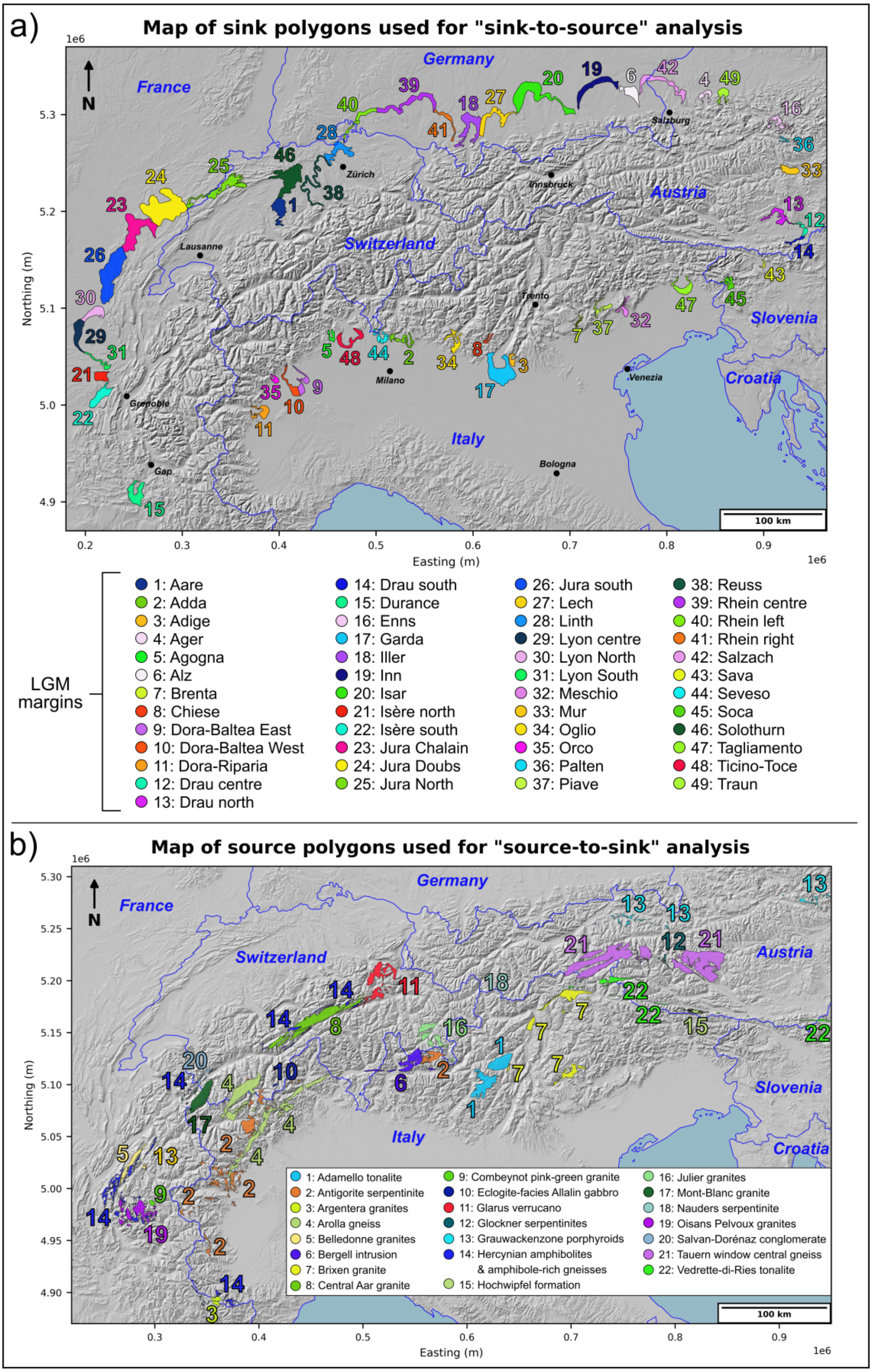

Figure 3. Maps of all sink and source polygons used for producing both catalogues of (a) sink-to-source and (b) source-to-sink analyses and their resulting particle trajectories. Sink polygons (a; n = 49) were selected and mapped to represent terminal ice-contact deposits for all major outlet glaciers of the Alpine Ice Field during the Last Glacial Maximum, while source polygons (b; n = 22) were selected and mapped from geological data on surface outcrops for key lithologies across the Alps (more details in section 2.4). In this and all subsequent paper figures displaying geo-spatial data, X and Y coordinates are displayed as projected (unit: m) in the WGS 84 / UTM zone 32N (EPSG:32632) coordinate reference system.

Importantly, our 49 sink polygons (Fig. 3a) are not a precise map of terminal LGM ice-contact deposits preserved in the Alps. However, they are useful to produce a first-order estimation of possible LGM glacial trajectories for deposits located towards major outlet glacier margins, pre-erosion. Producing an Alps-wide, digital and open-access map of all preserved terminal ice-contact deposits dating to the LGM (e.g. Clark et al., 2018; Davies et al., 2020) has yet to be achieved in the Alps and is beyond the scope of this study. To estimate the relative contributions of various provenances to the total particle number found in a sink deposit, we divide our Alps-wide domain in 241 present-day hydrological catchments; obtained from the global HydroBASINS database (Lehner & Grill, 2013), and named based on catchment-specific river names (Figure S1). Our sink-to-source analysis produces a catalogue of modelled particle trajectories, estimated provenance fractions per basin, and statistics including glacial transport time and particle age (i.e. seeding year), for all particles found in each of the 49 sink polygons shown in Figure 3a. All results are produced separately for subglacial and supraglacial particle seeding, enabling us to compare the impacts of different sourcing mechanisms on glacial sediment transport histories and provenances.

For the source-to-sink analysis, we select sources that represent mapped outcrops of specific alpine surface lithologies, to estimate the glacial transport pathways of sediments from specific rock types between 40 and 18 ka, across the Alps. We focus on rock type as this enables us to compare modelled estimates against empirical data on ice-contact deposits (e.g. erratic boulders) of known lithologies and locations post-retreat (e.g. Braakhekke et al., 2020; Monegato et al., 2022). This requires identifying surface lithologies specific enough to be associated with mapped outcrops and uniquely recognisable through geological assessment of ice-contact deposits. The outcrops moreover need to cover a large-enough area for enough particle seeding to overlap them, given that a single grid cell is 90,000 m^2. To identify such lithologies, we use the open-access 1:500,000-scale geological map sheets 1 and 2 from the 'Structural model of Italy' (Bigi et al., 1990a; b). These maps present a relatively high spatial resolution, are easily accessible online and georeference-able, and provide a consistent naming convention of lithologies across the entire Alps. We also use geodata derived from the Geological Map of Austria 1:50.000 sheets 197 Kötschach and 198 Weißbriach for one extra lithology (i.e. the Hochwipfel formation) (Geologische Bundesanstalt Österreich, 2021a, b). We then isolate a subset of 22 surface lithologies referred to as our 'source polygons' (Fig. 3b). While these are not a comprehensive list satisfying the above criteria, they are spatially widespread and cover the main rock types described by investigations on LGM erratic boulders in the Alps. They include Mont-Blanc granite (Bussien Grosjean et al., 2018), Glarus Verrucano (Letsch et al., 2015), or Salvan-Dorénaz conglomerate (Capuzzo et al., 2003), for instance (Fig. 3b).

The source-to-sink analysis involves finding all particles seeded within our 22 source polygons during the AIF simulations, and in mapping their glacial transport pathways. Due to existing mechanisms of sediment melt-out and lodgement at the ice-bed interface (Alley et al., 1997), we consider any location along the resulting trajectories to be a possible destination for glacial sediment of the studied lithology. Thus, the source-to-sink analysis produces a catalogue of maps displaying modelled trajectories of particles seeded within each of the 22 selected surface lithologies shown in Figure 3b. The maps are produced for both subglacial and supraglacial particle seeding allowing for a direct comparison between the two.

Consequently, the main outputs of this study are the ‘sink-to-source’ and ‘source-to-sink’ analyses, i.e. two catalogues of model results shared under the form of maps displaying source and sink particle trajectories, pie charts of deposit provenance fractions, histograms showing data from sink particles, and polyline shapefile data for visualization in GIS software. These data are all accessible from the Zenodo repository attached to this paper (link: https://doi.org/10.5281/zenodo.18374156).

3 Results

3.1 GPUs reduce the computational cost of particle tracking

GPUs are particularly well-suited for particle-based numerical modelling, such as Lagrangian particle tracking, due to their architecture which is optimized for massively parallel execution of small, independent computations, ideal for processing individual particles concurrently. This contrasts with traditional computing on Central Processing Units (CPU) which restricts the parallelization of such small operations on much fewer cores. Consequently, GPU-accelerated algorithms for particle-based modelling have been extensively developed in fields as varied as fluid mechanics, graphics, or geosciences (e.g. Wang et al., 2022; Aaron, 2023). In our specific application, we find that transferring all computation on the GPU makes 3D Lagrangian particle advection highly efficient, with a computational cost that remains small even when tracking tens of millions of particles within a modelled glacier (Fig. 4).

To quantify this gain, we ran a test simulation over the majority of the European Alps and, after initializing an LGM Alpine Ice Field (AIF), seeded new particles in all grid cells of the glacier accumulation area every two model years, thus quickly multiplying the total particle number. When operating on a single GPU (Nvidia RTX 4090), raising the number of particles from 0 to 50 million increases the mean cost of computing their advection linearly between 0.02 and 0.1 seconds per timestep (Fig. 4). Even with 50 million particles in the system, the computational cost of particle tracking remains below 26% of the mean cost (i.e. ~0.39 seconds per timestep) of all other IGM processes and modules in our Alps-wide simulation of the LGM at 300 m resolution. When running the same test using multiple CPUs instead, the mean costs of tracking 50 million particles reach approximately 26 and 5.5 seconds per timestep using 12 and 60 CPU threads, respectively (Fig. 4). These computational costs are between 274 and 55 times greater than those obtained with a single GPU, respectively. For 10 million advected particles, the costs are still 200 and 42 times greater than with the GPU, respectively. This shows that when using any traditional CPU-based glacier evolution model, coupling Lagrangian tracking of large particle numbers (>10^7) would substantially increase the simulation's computational cost. The alternative of accurately computing particle trajectories using post-processing only (after simulations are run), although not computationally restrictive, would be made impossible by the data volume of transient 3D velocity fields that would need to be saved at every time step (0.01-0.04 yr), which in our case would quickly exceed the hundreds of Terabytes. Contrastingly, when using IGM and a GPU-based approach, 3D particle tracking of large particle numbers can be coupled to simulations with only a small additional cost relative to the ice-flow model (Fig. 4). This enables us to run IGM simulations at high (300 m) spatial resolutions with millions of particles tracked over Alps-wide and multi-millennial scales, an experiment that would be unfeasible using traditional CPU-based computing.

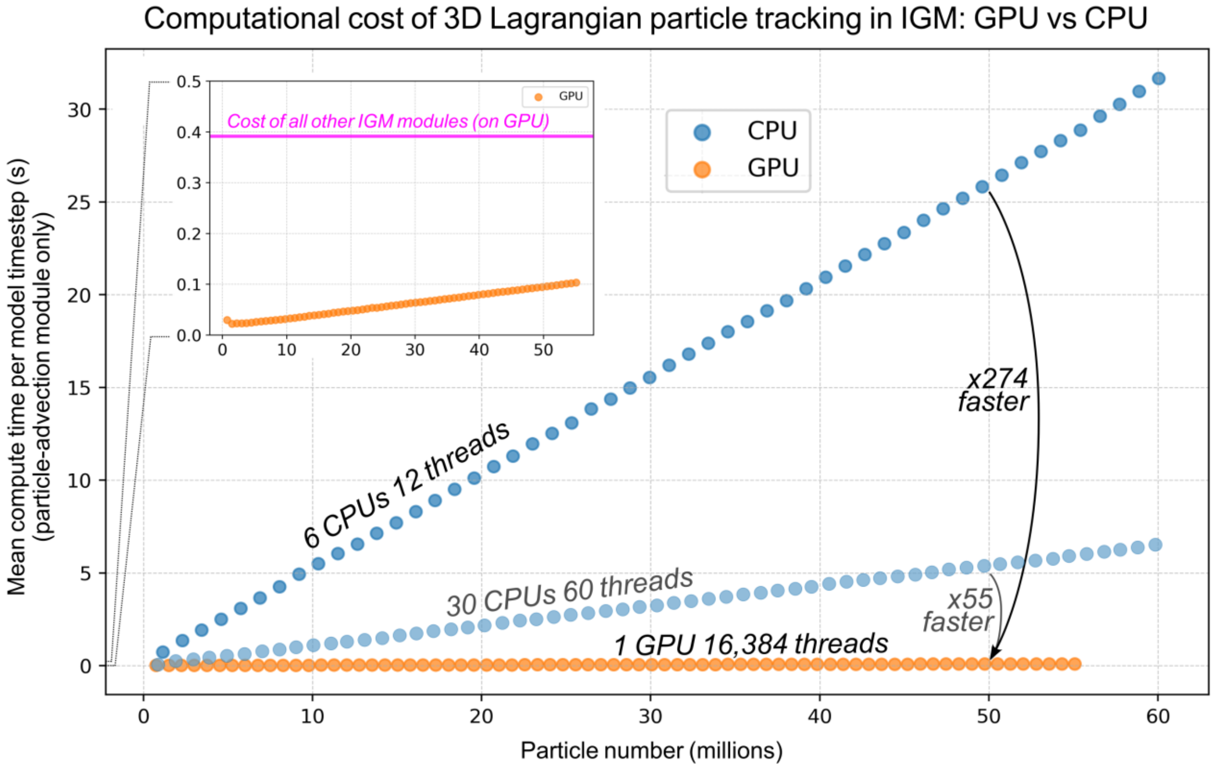

Figure 4. Mean computational time/cost (in seconds) of computing the Lagrangian 3D advection of particles in ice during a single model timestep of our Alpine-Ice-Field simulations with the Instructed Glacier Model (IGM), as a function of particle number. The data shown here allows one to compare the computational cost of Lagrangian particle tracking on a single GPU (orange dots; Nvidia RTX 4090) relative to computing it on multiple CPU cores (blue dots; Intel(R) Xeon(R) CPU E5-2620 v3). The difference between blue and orange dotted lines highlights the significant computational gain of parallelizing particle advection operations on the GPU. The intermediate line of blue dots (30 CPUs, 60 threads) is shown with slight transparency as numbers were calculated assuming linear proportionality to the real computational costs obtained with a 6 CPU (12 threads) setup. The inset graph changes the Y scale and zooms inside compute time values <0.5 seconds, allowing one to visualize the linear increase in cost with increasing numbers of advected particles when using the single GPU (otherwise invisible). The inset also compares this particle-module cost against the average computational cost (~0.39 s: pink line) of a single model timestep when combining all other GPU-based IGM modules used when running the Alps-wide 300 m best-fit simulation of Leger et al. (2025): i.e. the same simulation we re-run in this study.

3.2 Alps-wide patterns of glacial sediment sourcing

Our coupled glacier-particle simulations output a database of 3D particle coordinates and other statistics from the moment of seeding until the end of the glacier simulation (i.e. 18 ka). Thus, for both simulations with subglacial and supraglacial particle seeding, a map of seeding locations for each of the ~20.5 million advected particles can be produced. To visualize the spatial heterogeneity of particle seeding, we transform the seeding location data into normalized seeding density maps (Fig. 5). In Figure 5, bright colours (normalized density closer to 1) show regions with relatively more particle seeding events during the simulations. For subglacial seeding, these regions are associated with high basal ice velocities modelled during extended periods of the simulation, spanning 40-18 ka. These can be interpreted as likely to produce the largest volumes of glacial sediments of subglacial origin (e.g. abrasion and plucking) during the LGM. Potent subglacial sediment sourcing regions include the Rhône valley between Montreux and Sion (Switzerland), the Dora Baltea valley between Aosta and Ivrea (Italy), the Romanche valley between Le Bourg-d'Oisans and Grenoble (France), or the Rhein valley between Domat/Ems (Switzerland) and Bregenz (Austria), for instance (Fig. 5a).

For supraglacial seeding, regions of high seeding densities are those presenting steep topographies (>45°) and ice-free conditions (or thin ice cover: <20 m) during extended time-periods of the simulation. These regions also need to be near dynamic modelled glaciers for seeded particles to eventually get transported by glacier ice. These regions are interpreted as likely to have produced the largest volumes of supraglacial sediments (e.g. from rockfall, debris flow, landslides, avalanches) during the LGM. Our results suggest that high supraglacial sediment sourcing regions are widespread (Fig. 5b) but include, for instance, the Écrins Massif (France), the Lepontine Alps (Switzerland), the Dolomiti Bellunesi Massif (Italy), the Triglav Massif (Slovenia), or the Bernese Alps (Switzerland). During the LGM, these regions are most concentrated within a narrow band located towards the northern and southern peripheries of the alpine arc, where high-elevation terrain (> 2500 m a.s.l.) combined with thin/no ice cover maximize the likelihood of nunatak occurrence (Fig. 5b). Contrastingly, supraglacial sediment sourcing is lower further towards the Alps' interior, where the model produces greater ice thicknesses and topographic ice covers for extended periods, thus reducing nunatak occurrence.

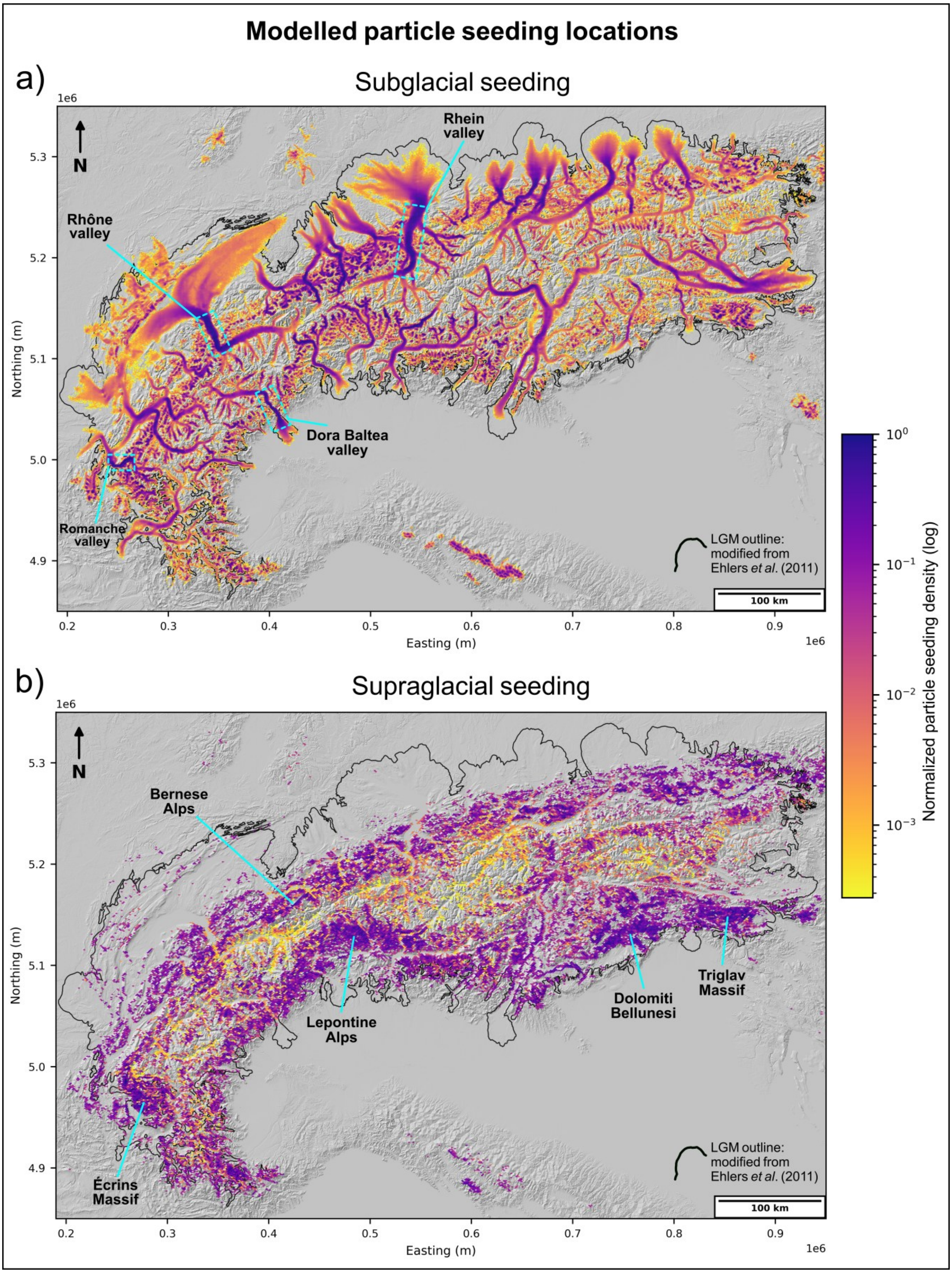

Figure 5. Maps showing the seeding locations of all modelled particles (~20.5 million at maximum) in both simulations with (a) subglacial and (b) supraglacial particle seeding. The maps are divided into small hexagons in which the total number of seeded particles is computed. Hexagons are colored based on this total number normalized across the entire dataset, resulting in a density map of particle seeding locations, with brighter yellow colors indicating relatively more seeding, and darker purple colors indicating relatively less seeding. A lack of colors (grey hillshade background) indicates no particle seeding occurred at any time during simulations.

3.3 The sink-to-source analysis and catalogue

With the sink-to-source analysis, we produce a catalogue of modelled time-transient trajectories for terminal LGM ice-contact deposits mapped across the Alps, hereafter referred to as our 'sinks' (see section 2.4). Sink-to-source trajectories reveal the modelled pathways of ice-advected particles ending up within these sinks after final glacier retreat. For each sink polygon mapped (n = 49; Fig. 3a), we provide a high-resolution map of particle trajectories, along with an estimation of particle provenance fractions, i.e. the proportions of sink particles originating from specific hydrological basins (see section 2.4; Figure S1). For each sink and particle in this sink, we also produce statistics on total particle glacial transport distance, cumulative glacial transport time, cumulative time in ice-free conditions during source-to-sink journey, and seeding year (i.e. timing of erosion). These data are produced for both cases of subglacial and supraglacial seeding, enabling us to quantify differences in glacial transport dynamics between the two. We consider the sink-to-source catalogue to be a main result of this study and encourage readers to download it from the Zenodo repository attached to this paper (link: https://doi.org/10.5281/zenodo.18374156). All particle trajectory data for each seeding type and sink are also available as polyline shapefiles for visualization in GIS software.

3.3.1 A sink-to-source case study: the Inn glacier LGM margins

As a case study, we here describe the results of our sink-to-source analysis for a single ice-contact deposit, i.e. the Inn glacier LGM margins (sink 19; Fig. 6). We chose this outlet glacier as its modelled ice-flow during the LGM originates from a large variety of catchments, produces numerous transfluences, has been the subject of several studies (e.g. Reitner, 2007; van Husen, 1997), and produces a good ice-extent fit during maximum expansion with empirical data (see Fig. 1a in Leger et al., 2025). In our subglacial and supraglacial seeding simulations, totals of 53,797 and 36,945 particles end up within this ice-contact deposit, respectively (Fig. 6). The sink particles originate from 15 (for subglacial seeding) and 12 (for supraglacial seeding) different hydrological basins. Our modelling suggests the basin contributing the most ice-contact sediments of subglacial origin is the Inn-Simsee basin (basin 44; Figure S1), with an estimated provenance fraction of 42.5% (Fig. 6). For supraglacial seeding, the distribution of provenance fractions is different. The basin estimated to provide the most sediments of supraglacial origin is the Ziller basin (basin 191; Figure S1), although its provenance fraction (32%) is tied with the Alz-Traun basin (basin 63, 29.5%). On average, our modelling suggests that ice-contact deposits of the LGM Inn glacier margins spent 3,021 yrs (interquartile range (IQR) = 4,114 yrs) in glacier ice for those of subglacial origin. This median number is approximately twice greater for ice-contact deposits of supraglacial origin, with a cumulative glacial transport time of 6,361 yrs (IQR = 3,641 yrs) (see section 3.3.2 for why). At maximum, particles are modelled to spend up to 12,644 and 14,613 yrs in ice for subglacial and supraglacial seeding, respectively (Fig. 6e, f). Particles yielding such high glacial transport times are few (<300) and frequency distributions tail off, which indicates that starting our simulations at least 15 kyr before the local LGM (~24.8 ka) is both important and adequate (Fig. 6e, f). On average, ice-contact deposits of the Inn LGM margins are modelled to have travelled over 78 km (IQR = 80 km) and 138 km (IQR = 81 km) for sediments of subglacial and supraglacial origin, respectively. Ice-contact deposits of subglacial origin are estimated to have spent, on average, a total of 353 yrs (IQR = 1,936 yrs) in ice-free conditions during their source-to-sink journey. This time in ice-free conditions occurs when particles are deposited following temporary ice retreat, prior to re-entrainment by subsequent advances (see videos in supplement). This median number increases fivefold to 1,885 yrs (IQR = 3,719 yrs) for sediments of supraglacial origin, suggesting a greater potential for atmospheric exposure during their transport (assuming they remain at the Earth's surface). In line with these estimations, the results suggest that ice-contact deposits of the Inn LGM margins and of supraglacial origin are on average eroded 5,090 yrs earlier than those of subglacial origin (Fig. 6).

For these Inn glacier LGM margin deposits, the modelled trajectories of subglacially-seeded sediments display similar pathways than those of supraglacial origin. However, we find that glacial sediments of supraglacial origin, due to reaching glacier surfaces from nunataks and valley/glacier sides, are more likely to produce trajectories resembling well-defined medial moraines (e.g. Fig. 6b, basins 170, 150). We find this is rarely the case for modelled trajectories of subglacially-seeded particles, which can originate from across the glacier bed, including from valley/glacier centres where basal velocities are highest. This difference also explains why subglacially seeded particles spread over the entire terminal perimeter of the Inn glacier's piedmont lobe during the LGM. However, particles of supraglacial origin rarely reach the glacier's centreline and are pushed sideways by flow divergence within the piedmont lobe, causing preferential advection to both the left and right lateral margins of the terminal lobe, but not to its centre (Fig. 6). We observe a similar trajectory differentiation between ice-contact deposits of subglacial versus supraglacial origin for the Garda (sink 17) and the Ticino-Toce (sink 48) outlet glaciers, towards their modelled piedmont lobes (see 'sink-to-source' catalogue). This mechanism has important implications for sampling frontal moraines for detrital thermochronology and linking sampling locations to catchment provenances (e.g. Bernard et al., 2020).

These results focus on a single LGM ice-contact deposit, or 'sink', as an example. The same data were obtained for all 49 mapped sinks (Fig. 3a) and can be viewed via the sink-to-source analysis catalogue (link: https://doi.org/10.5281/zenodo.18374156).

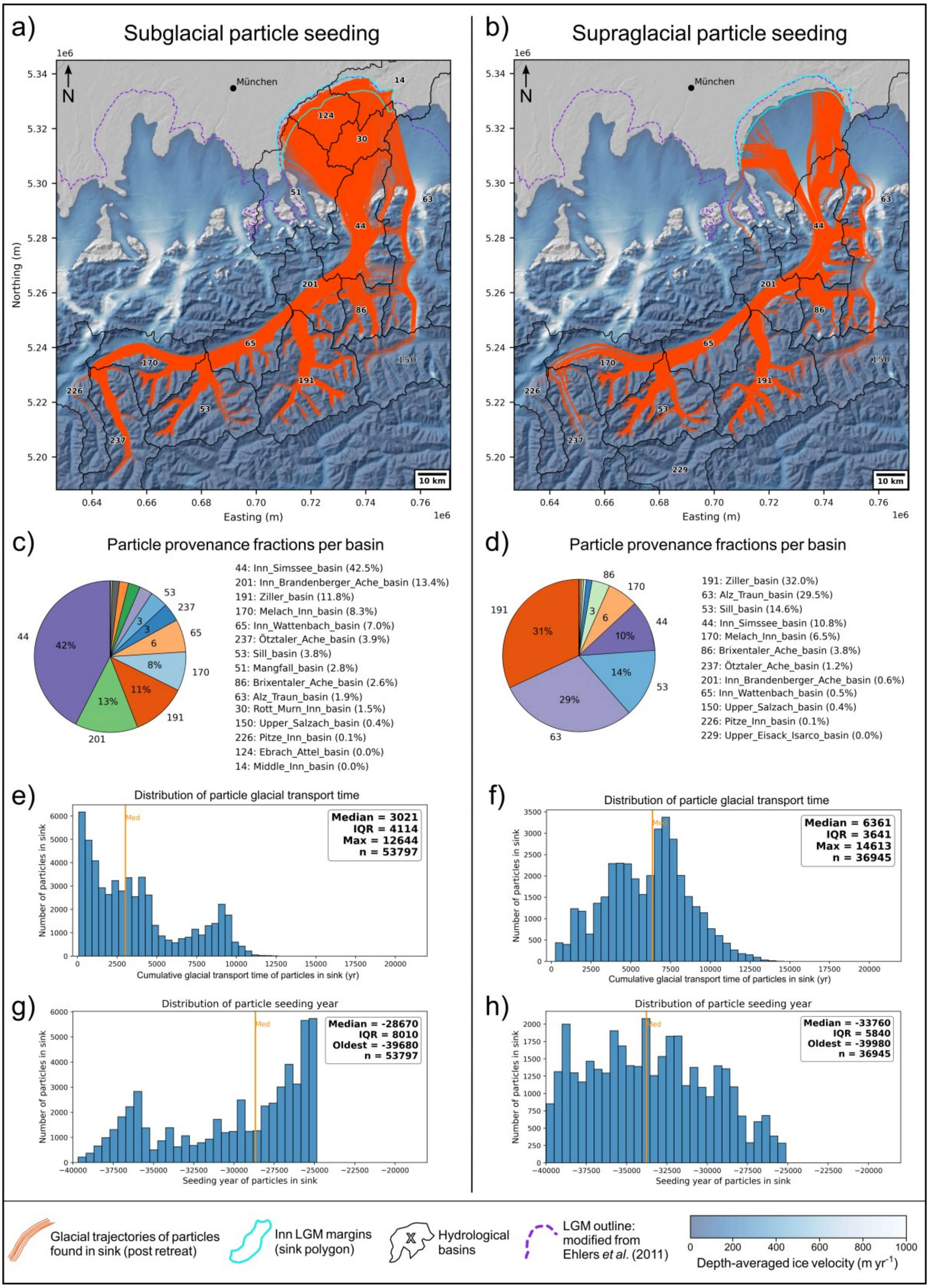

Figure 6. Sink-to-source analysis and resulting modelled particle trajectories (a, b) and transport statistics (c-h) for subglacially (a, c, e, g) and supraglacially (b, d, f, h) seeded particles ending up in the chosen sink (cyan polygon) following final glacier retreat. Here, results are shown for a single example sink (or ice-contact deposit) from our sink-to-source catalogue (n=49 sinks in total), i.e. the Inn glacier LGM margins (sink 19: see Fig. 3a for location). The pie charts (c, d) and associated legends indicate the provenance fractions of all particles ending up in this sink for each hydrological basin (mapped and numbered in black on panels a, b) in which they were seeded (see Figure S1). Histograms (e-h) display the resulting distributions of sink particle cumulative glacial transport times and seeding years (i.e. particle age). 'IQR' stands for 'Interquartile Range': i.e. the spread of middle 50% of the dataset: 75th - 25th percentiles.

3.3.2 Ice-contact deposits of subglacial versus supraglacial origin

As described above for Inn glacier LGM deposits, we find notable differences in glacial transport histories and characteristics between ice-contact deposits of subglacial versus supraglacial origin. Similar differences hold true when analysing all 49 sinks and the 3.1 million particles deposited within them (Fig. 7). For the majority of these sinks (41 out of 49), cumulative glacial transport time is on average greater for particles of supraglacial origin. When averaging across all of the sinks, the glacial transport time for particles of supraglacial origin is higher than for those of subglacial origin by approximately 1,925 years, i.e. a factor of 1.9 increase. The total ice-free time (pre-deposition) of sink particles during their source-to-sink journey is also higher for those of supraglacial origin in 41 out of 49 cases, and on average by 1,519 yrs, a factor of ~2.74 increase (Fig. 7). We find a similar pattern for the age (i.e. the seeding year) of sink particles, which is older (on average by 4,640 yrs) for those of supraglacial origin in 46 out of 49 cases. Thus, our modelling suggests that in the Alps, LGM terminal ice-contact deposits of supraglacial origin were likely to be eroded earlier in time, spend more time in or on glacier ice, and spend more time exposed in ice-free conditions during their full source-to-sink journey (Fig. 7). This is likely caused by glacial sediment of supraglacial origin reaching the glacier surface mainly in accumulation areas, where steep topographies protrude, and where ice velocities are lower.

Unlike subglacially-eroded materials which are preferentially produced in fast-flowing areas often located closer to terminal deposits, supraglacial debris requires (on average) more time to be advected to lower glacier elevations and areas of faster-flowing ice and, in turn, to the terminus. Moreover, glacial sediments of supraglacial origin tend to reach contact with ice towards slope-adjacent glacier sides, making them likely to remain near lateral ice margins during glacial transport. This increases their chances of deposition during temporary periods of ice retreat and thinning, which can increase their cumulative ice-free time during their source-to-sink journey. In contrast, subglacially-eroded sediments will preferentially be concentrated towards the faster-flowing centreline of glaciers, further away from lateral glacier margins. These results have implications for terrestrial cosmogenic nuclide exposure dating of moraine sediments deposited by alpine glaciers and other topographically constrained icefields (Heyman et al., 2011). Indeed, they imply that ice-contact deposits of supraglacial origin are more likely to yield cosmogenic nuclide inheritance signals relative to those of subglacial origin, not only because of pre-transport exposure, but also due to potentially longer and more complex glacial transport histories. However, one must note that clast erosion during glacial transport can counterbalance this mechanism and instead remove nuclide inheritance signals (Matthews et al., 2017) (more details in Discussion).

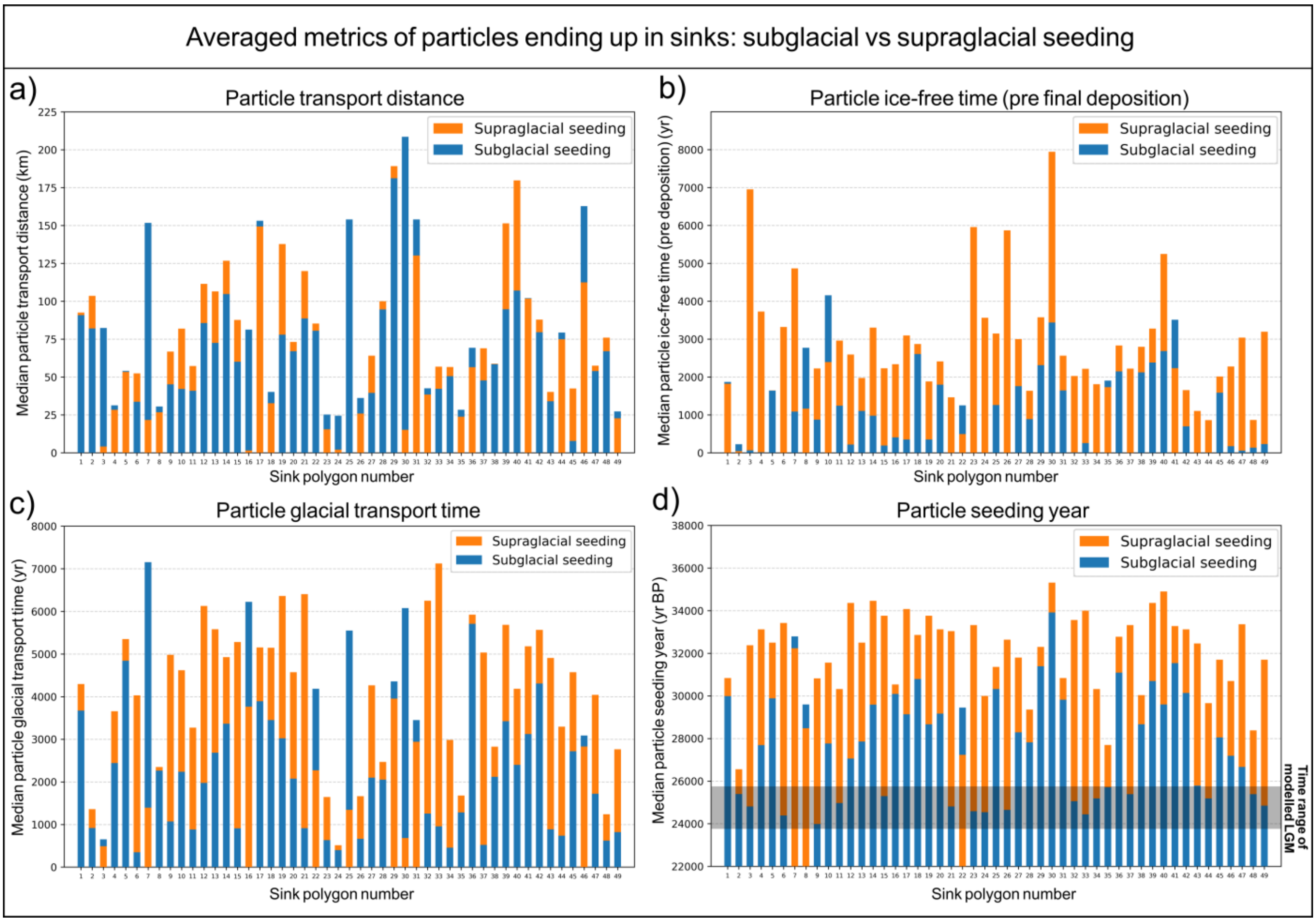

Figure 7. Overlapping bar plots (non-stacked) indicating particle statistics averaged over all sink particles (median) for each of the 49 sinks (or ice-contact deposits) in our catalogue (x axis), shown separately for both subglacial seeding (blue bars) and supraglacial seeding (orange bars). See Fig. 3a (or catalogue) to visualize the locations and names of these 49 sinks. The data are shown for four distinct particle metrics, i.e. the median sink particle transport distance (a), the median cumulative time a particle spent in ice-free conditions during its full source-to-sink journey (b), the median cumulative particle glacial transport time (c), and the median particle seeding year (i.e. the particle age) (d). For all metrics except transport distance, modelled sink particles of supraglacial origin tend to display higher median values (orange bars taller than blue bars), suggesting that, on average, they tend to be older (i.e. seeded earlier), spend more time in glacier ice, and spend more time in ice-free conditions during their source-to-sink journey, relative to sink particles of subglacial origin.

3.3.3 Addressing ‘sink-to-source’ debates: The Mont Salève erratics case study

To demonstrate that our modelled glacial sediment trajectories can help address tangible research questions and scientific debates in the Alps, we conduct a specific analysis for the example of the Mont Salève erratics. The Mont Salève, located 10 km to the south of Geneva, is a ~600 m tall, ~16 km long, and ~2.5 km wide limestone mountain part of the Jura Massif. The Salève features a flat plateau-like summit (~1300 m a.s.l.) displaying approximately 400 preserved erratic boulders (1200 pre-exploitation) officially protected since 1877 and subject to investigations since (e.g. Coutterand, 2010). Some of the erratics were geologically identified as Gneiss from the Siviez-Michabel nappe (Valais, Switzerland) while others as Mont-Blanc granite. They were hypothesised to have been deposited during retreat phases and thinning from the largest Late-Pleistocene glaciations of the AIF. More specifically, Coutterand (2010) attributed their glacial transport and deposition to two separate glacier systems; i) the Rhône glacier flowing along the Rhône valley and Geneva Lake basin thus reaching the Salève from the northeast, and ii) the Arve glacier flowing along the Arve valley and originating from the Mont-Blanc Massif thus reaching the Salève from the southeast. Our study enables to compare these hypotheses against modelled estimates. Firstly, our results suggest the Mont Salève summit was covered by a thin (~30 - 100 m) layer of ice during the LGM, when peak AIF extent and volume was reached (~24.8 ka; Leger et al., 2025) (Fig. 8). When tracking the trajectories of all particles deposited on the Mont Salève following deglaciation, we find that no particles are modelled to be deposited by the Arve glacier (Fig. 8). Instead, between 40 and 18 ka, 100% of modelled ice-contact deposits on the Salève are deposited by the Rhône glacier, with glacial sediment travelling exclusively along the western side of the Rhône valley and the southern side of the Geneva Lake basin (Fig. 8). The seeding locations of particles deposited on the Salève trace back to the northeastern sectors of the Mont-Blanc Massif, thus overlapping Mont-Blanc granite outcrops, but also to the Dranse de Bagnes, Dixence, and Val-d'Hérens valleys (Vallais, Switzerland) thus overlapping the Siviez-Michabel gneiss nappe (Bigi et al., 1990) (Fig. 8). Thus, in our simulations, the geographical origin of both subglacially- and supraglacially seeded particles can explain the lithologies of erratic boulders found on the Salève plateau (Fig. 8).

The lack of Salève-deposit trajectories associated with the Arve glacier is related to the modelled dynamics of confluence between the Rhône and Arve glaciers. Our simulations suggest that during the last AIF advance preceding the LGM (~28-26 ka), a branch of the more voluminous and thicker Rhône glacier expanded southward from the Geneva Lake basin into the Arve valley and around the southeastern flanks of the Salève. This modelled expansion generates enough driving stress to push the thinner Arve glacier, forced to redirect its flow south-westward due to its lower ice discharge rate (Fig. 8). Consequently, our simulations suggest the Mont Salève remained surrounded by ice exclusively from the Rhône glacier during the LGM and until final deglaciation from the area (~20 ka in our simulations). More empirical investigations and dating of the Salève erratics are needed to either validate or discard this new model-derived hypothesis, which differs from the previous empirical hypothesis (Coutterand, 2010). Regardless, this study case of the Mont Salève erratics is a prime example demonstrating how Alps-wide modelling of glacial sediment transport can help address questions on past glacier flow dynamics and the former transport history of certain ice-contact deposits.

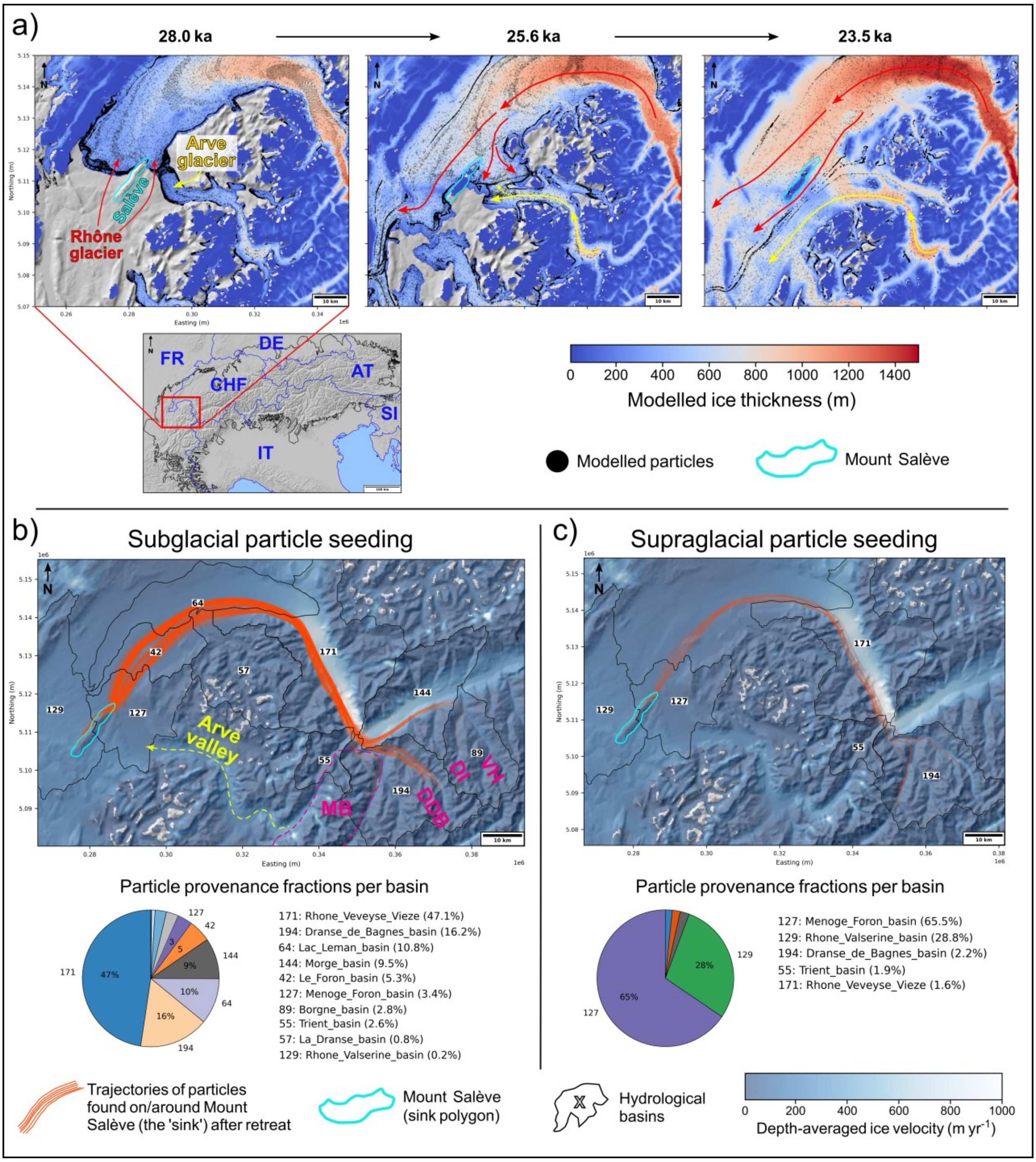

Figure 8. Instructed Glacier Model (IGM) output, sink particle trajectory maps, and sink particle provenance fractions per hydrological basin, for the Mont Salève erratics case study (see section 3.3.3). The three ice-thickness model output snapshots (a) at 28, 25.6, and 23.5 ka display the modelled ice thickness fields in the region of the Mont Salève (location relative to the Alps indicated by small inset featuring a hillshade and country borders), indicating how the Rhône and Arve glaciers interact in our model. More specifically, they show how, in our simulation, the Rhône glacier pushes the ice from the Arve glacier towards the southwest forcing it to redirect its flow: causing the Mont Salève to be surrounded by modelled ice exclusively from the Rhône glacier during the entire Last Glacial Maximum (LGM). This in turn explains the resulting particle glacial-transport trajectories (b, c), highlighted by orange lines, shown for particles ending up on and around the Mont Salève following final ice retreat. These suggest no ice-contact deposits of the Mont Salève are modelled to be transported by the Arve glacier. They are instead all exclusively transported by the Rhône glacier. Note particle seeded within Basin 129 (28% of particles for supraglacial seeding) are only local to Mont Salève: i.e. particles from near the summit moved downslope and which still end up within the mapped polygon following final ice retreat. On panel b; 'MB', 'DDB', 'DI', and 'VH' stand for the 'Mont-Blanc Massif', and the 'Dranse de Bagnes', 'Dixence', and 'Val-d'Hérens' valleys, respectively, enabling to locate places mentioned in main text (section 3.3.3).

3.4 The source-to-sink analysis and catalogue

With the source-to-sink analysis, we produce a second catalogue of time-transient (40-18 ka) glacial sediment trajectories for a selection of key surface lithologies across the Alps, hereafter referred to as our 'sources' (see section 2.4) (link: https://doi.org/10.5281/zenodo.18374156). These trajectories reveal the pathways of particles seeded either subglacially or supraglacially within source polygons (n = 22; Fig. 3b). For each source polygon and seeding type, we provide a high-resolution map of source particle trajectories. We interpret these source-to-sink trajectories as model estimates of possible locations (along the modelled trajectories) where sediments of a specific surface lithology may have been transported to and deposited by ice between 40 and 18 ka. These locations can then be compared against the coordinates of documented deposits (e.g. erratic boulders) of known lithology, which may help assess the accuracy of our modelling.

3.4.1 A source-to-sink case study: the 'Arolla Gneiss' trajectories

As an example from our catalogue, we here describe our source-to-sink analysis for a single lithology, i.e. Arolla Gneiss (source number 4 in the catalogue: Fig. 9). This lithology is part of the Austroalpine system of the western Alps and, more specifically, of the Dent Blanche and Sesia Lanzo composite nappe-system of Paleoafrican provenance (Manzotti, 2011). It was formed during the Early-Alpine and Lepontine tectonometamorphic events and is mainly composed of greenschist orthogneisses from Late-Hercynian granitoids (Bigi et al., 1990a). This lithology outcrops mainly within the Dent Blanche, Dent d'Hérens and Weisshorn Massifs (Swiss Alps), and along a narrow band of the southern Italian Alps stretching for ~160 km from the Valle di Viù to the Melezza valley and Locarno (Ticino, Switzerland) (Fig. 9). Numerous erratics deposited in the Swiss and Italian alpine forelands are of Arolla-Gneiss lithology (e.g. Graf et al., 2015).

In our simulations, Arolla Gneiss is modelled to be eroded and transported by ice into vastly different valleys and outlet glacier catchments following diverse and complex trajectories (Fig. 9). It is for instance modelled to be transported by the Rhône outlet glacier reaching the Lyon outlet glacier (France), but also by the Solothurn outlet glacier (Switzerland), the Dora Baltea outlet glacier reaching the Ivrea morainic arc (Italy), and the Ticino-Toce outlet glacier (Italy) (Fig. 9). Arolla Gneiss trajectories enable us to visualize how modelled ice flux from the upper Rhône glacier diverges over the northern Lake Geneva flanks during the LGM, as previously modelled (e.g. Jouvet et al., 2017). Indeed, it reveal how modelled ice flowing along the true right side of the Rhône valley (between Martigny and Montreux, Switzerland) bends eastwards and heads towards Solothurn, while ice flowing along the true left side of the Rhône valley bends south-westwards along the Geneva Lake and heads towards the Lyon outlet glacier (Fig. 9).

Interestingly, some of the particles heading towards Solothurn are pushed against the southeastern Jura flanks in locations of modelled ice transfluences causing glacial transport through the Jura mountains, into the Doubs valley and towards the northern margins of the Jura icecap (France) (Fig. 9). Our simulations thus produce transfluences of alpine ice overflowing the Jura mountains during peak LGM extent and volume (~24.8 kyr). These transfluences are modelled in three broad locations, firstly towards the Vallorbe pass and the valley of the Jougnena (46°43'N; 6°23'E), secondly towards Baulmes and Sainte-Croix (East of the Mount Suchet: 46°48'N; 6°30'E), and thirdly directly West of Vallorbe over the 'Grotte aux Fées' cave and the Combe du Puits area (46°42'N; 6°19'E). Former expansions of alpine glaciers overflowing the Jura mountains are thought to have occurred during pre-LGM maximum Late-Quaternary glaciations such as during Marine Isotope Stage (MIS) 12, 10, 8, or 6 (Keller and Krayss, 2011; Preusser et al., 2011; Graf et al., 2015; (Mathes et al., 2026)). However, no published evidence yet exists for such transfluences during the LGM (MIS 2) (Campy, 1992; Buoncristiani & Campy, 2011). Our model may either slightly overestimate ice thickness over the Rhône and Solothurn glaciers during the LGM, or may be correct but sedimentological evidence for such momentary transfluence may be rare and not yet documented/dated. In either case, our high-resolution modelling helps target field sampling locations more precisely by producing particle trajectories that inform physically-plausible transfluence locations. The modelled Arolla-Gneiss trajectories reveal other surprising and complex pathways, such as possible transport of glacial sediments up into the Aulps valley (Morzine river valley, France) by ice from the Rhône glacier which, in our model, generates southward ice-flow upvalley from the Geneva Lake basin (Fig. 9). Key differences can be observed between modelled Arolla-Gneiss trajectories of particles seeded subglacially versus supraglacially. Within the Rhône glacier catchment, Arolla-Gneiss outcrops are confined to high-elevation topographies located towards the glacier's upper accumulation zone, where nunatak occurrence and rockfall potential are high, and where modelled basal ice velocities remain relatively low (<50 m yr^{-1}). Thus, within the Rhône glacier catchment, supraglacially seeded particles from Arolla-Gneiss outcrops yield a higher number and diversity of modelled trajectories, relative to subglacially-seeded particles (Fig. 9). In the southern Italian Alps, particle trajectories show the opposite, with numerous outcrops located in fast-flowing ice regions leading to higher numbers of trajectories and ice-contact deposit locations for particles of subglacial origin.

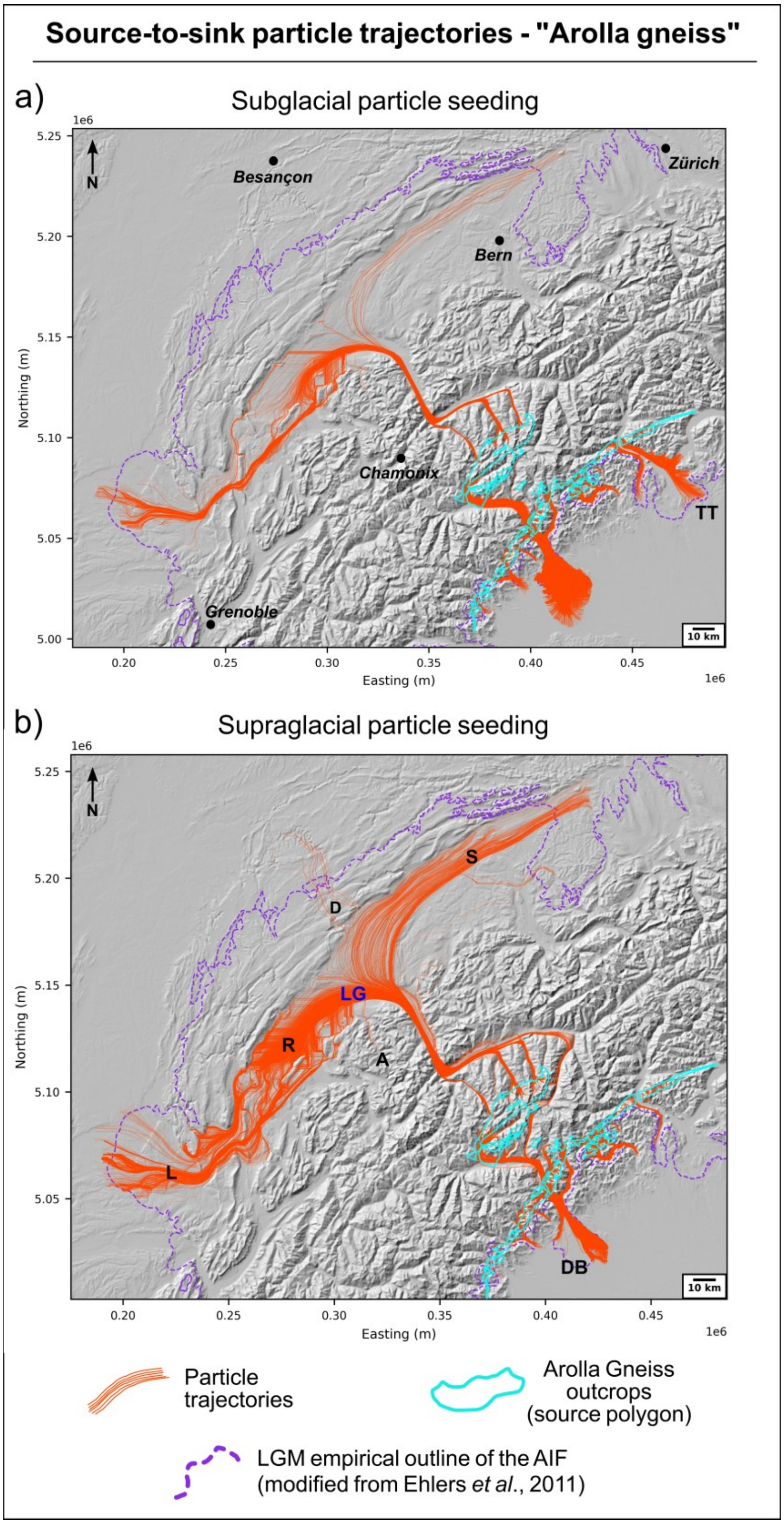

Figure 9. Source-to-sink analysis and resulting particle glacial-transport trajectories for all particles seeded within an example source polygon; in this case a single surface lithology from our source-to-sink catalogue (n=22 surface lithologies), i.e. the Arolla Gneiss (originally mapped by Bigi et al., 1990). Particle trajectories are shown for both subglacial (a) and supraglacial (b) seeding. We interpret these source-to-sink trajectories as model estimates of possible locations (along the entire trajectories) where ice-contact deposits of the Arolla-gneiss lithology may have been transported to and deposited by glaciers between 40 and 18 ka (time frames of simulations). The labels 'A', 'DB', 'D', 'L', 'LG', 'R', 'S', 'TT' stand for: 'Aulps valley', 'Dora-Baltea outlet glacier', 'Doubs valley', 'Lyon outlet glacier', 'Lake Geneva', 'Rhône glacier', 'Solothurn outlet glacier', 'Ticino-Toce outlet glacier', respectively, and relate to places/features mentioned in the main text (section 3.4.1).

3.4.2 Model-data comparison with dated erratics

Our 'source-to-sink' analysis provides the opportunity to test model agreement against data from ice-contact deposits of known provenance. Here, we conduct such a model-data comparison by compiling peer-reviewed publications which dated erratic boulders in the Alps to the time range of our simulations (40-18 ka) using terrestrial cosmogenic nuclide exposure dating (Table S1). The compiled erratics need to feature a lithological description that is specific enough (e.g. 'Central Aar granite') to be associated to a well-defined and spatially restricted lithology (unlike 'limestone', for instance). Moreover, only one sample per location (i.e. a sampling site in original studies) is considered for this test, to reduce statistical biases. A total of 38 erratic boulders were found to match these requirements, published in 13 separate studies (Ivy-Ochs et al., 2004; Gianotti et al., 2008; Reber et al., 2014; Graf et al., 2015; Bichler et al., 2016; Wüthrich et al., 2018; Ivy-Ochs et al., 2018; Boxleitner et al., 2019; Prud'homme et al., 2020; Braakhekke et al., 2020; Kamleitner et al., 2022; Kamleitner et al., 2023; Roattino et al., 2023). Exposure ages were re-calculated consistently as part of the AlpIce geochronological database (Kamleitner et al., *in prep*). Modelled particle trajectories (subglacial and supraglacial seeding combined) for the relevant source lithology successfully overlap the locations of erratic boulders of that lithology in 26 out of 38 cases (Table S1). The trajectories thus fit empirical data in 68% of cases. This number would moreover increase to 81% would we tolerate a small (<4 km) increase in ice extent in locations where our model slightly underestimates ice extent during the LGM, relative to mapped terminal moraines (see Fig. 1a, 4a in Leger et al., 2025). Thus, clear model-data misfit is only observed in 18% of cases (10 boulder samples). These results suggest our LGM model of the AIF coupled with our particle-seeding and 3D tracking schemes can transport particles to appropriate locations, for the majority of the compiled erratics (Table S1).

3.5 Detecting LGM ice transfluences across the Alps

As shown above with the example of Arolla Gneiss 'source-to-sink' trajectories overflowing the Jura Massif, the coupling of 3D particle tracking enables us to estimate the precise locations and time span of ice transfluences in the Alps during the LGM (Fig. 10). Ice transfluences occur when the growth of ice sheets and/or icefields cause the formation of topographically uncoupled ice domes, i.e. which accumulate away from summits and hydrological catchment divides. If the surface elevation of these domes exceeds the altitude of neighbouring cols, uncoupling from main hydrological catchments occurs causing ice-flow to cross main hydrological divides (Linton, 1949). This can result in glacial sediment transport over high-elevations ridges/cols and into different catchments (Monegato et al., 2022) (Fig. 10). Reconstructing LGM transfluences can thus help understand former ice-flow dynamics and unravel the puzzling lithologies/provenances of certain ice-contact deposits in the Alps (e.g. Reitner et al., 2010). Here, we loaded our modelled particle trajectories and thus 3D ice-flow lines into a geographic information software (ArcGIS Pro 3.4) to detect the occurrence of ice transfluences in our simulations, focusing only on the 11 largest hydrological catchments of the Alps (Rhône, Aare, Rhein, Isar, Inn, Enns, Drau, Piave, Brenta, Adige, Po) (Lehner & Grill, 2013). We present the results of this analysis in a series of maps (Figures S8-14) highlighting the locations of modelled ice domes, flowlines, and ice transfluences across the Alps. Figure 10 shows one of these maps for the example region of the upper Inn catchment. There, the build-up of the 'Engadin' ice dome centred towards Zernez (46°41'N, 10°05' E, 1465 m a.s.l.) and reaching a modelled maximum ice surface elevation of ~3100 m a.s.l. leads to a complex network of topographically uncoupled flowlines causing a high concentration of ~30 ice transfluences into the adjacent Rhein, Adda, Adige, and Isar catchments (Fig. 10). This causes, for instance, modelled ice from the Inn valley between St.-Moritz (46°29'N; 9°50'E) and Zernez (a 45 km stretch) flowing south-westwards over the Maloja pass (46°24'N; 9°41'E) into the Val Bregaglia, Como Lake basin, and feeding the Adda and Seveso outlet glaciers (sinks 2 and 44 in 'sink-to-source' catalogue). As another example, we note that our model reproduces the well-documented Simplon pass transfluence (e.g. Florineth & Schlüchter, 1998; Kelly et al., 2004; Dielforder & Hetzel, 2014), with ice possibly transporting sediments from the Eiger-Mönch-Jungfrau mountains (e.g. Aar granites) across the Rhône valley, over the Simplon pass, and into the Ticino-Toce glacier system during the LGM (sink 48 in 'sink-to-source' catalogue, Figure S11). In our simulations, we also find that modelled ice is always warm-based towards the main ice domes and transfluences occurring during the LGM (see Fig. 6b in Leger et al., 2025). Moreover, the modelled time span of transfluence occurrence is highly case-specific and can vary from 1-3 kyr, thus only during peak LGM conditions (e.g. the Simplon pass transfluence), to up to nearly the full simulation time frame (i.e. 22 kyr) and LGM period (e.g. the Engadin ice dome, Fig. 10). Consequently, our results show that coupling 3D Lagrangian particle tracking to glacier evolution modelling can also help identify the detailed events of complex and momentary topographic uncoupling of ice-flow during major Quaternary glaciations of the Alps.

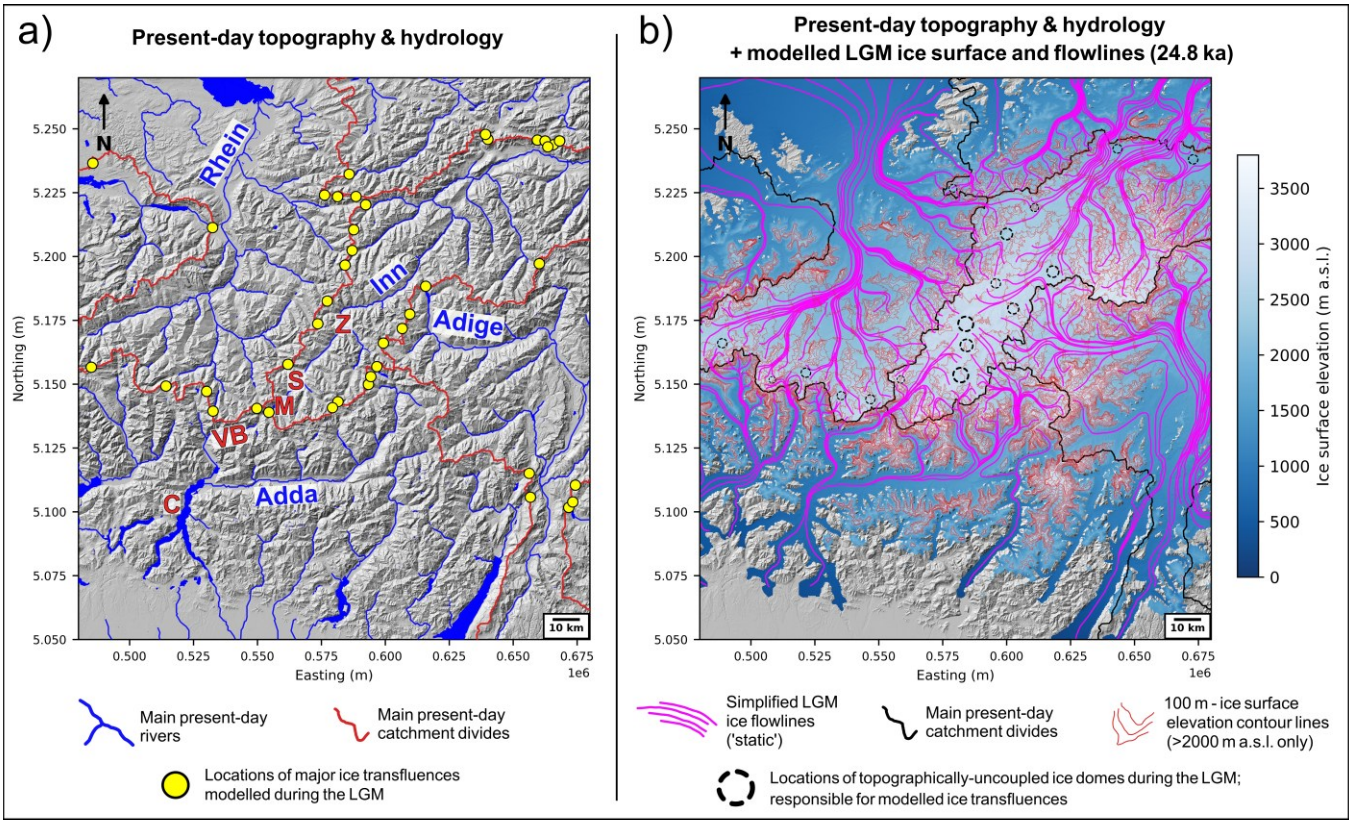

Figure 10. Map of modelled ice surface elevations and simplified 'static' ice flowlines (pink lines) during the LGM (~24.8 ka) in the region of the Engadin ice dome, with locations of modelled ice transfluences (yellow dots on panel a). These transfluences can explain the complex provenance of certain ice-contact deposits. We quantified them for the 11 largest river catchments of the Alps, whose divides are shown in red on panel a, and black on panel b. A series of six figures displaying the same ice-transfluence analysis for five other regions of the Alpine Ice Field (AIF) are available in the Supplementary Materials. Note that whilst useful for the visual purpose of this figure, the simplified glacier flowlines (pink lines) shown here (panel b) are drawn from so-called 'static' flowlines, which are non-time-transient and only obtained from the depth-averaged ice velocity field modelled during a single time frame: i.e. the maximum AIF volume; at 24.8 ka. These should only be considered useful to visualize the modelled flow direction of ice at the precise locations of transfluences and only during peak LGM. The substantially more complex and accurate time-transient flow trajectories obtained from our 3D Lagrangian particle tracking, displayed in Figures 6 and 9 for example, are more diverse and representative of the modelled time-transient ice-flow trajectories, but would make visualizing transfluences on this figure impossible given the large number of modelled particles and resulting cross-cutting trajectories (see Figure S7). On panel a, the 'C', 'M', 'S', 'VB', and 'Z' labels in red stand for 'Lake Como', 'Maloja pass', 'St. Moritz', 'Val Breglaglia', and 'Zernez', respectively, and relate to locations mentioned in main text (section 3.5).

3.6 Particle trajectory sensitivity to model parameters

To assess the sensitivity of our particle trajectories to both the seeding scheme and model parameters, we conduct two additional AIF simulations that differ from the original setup presented above like so: i) The first sensitivity test uses a 'simple' seeding scheme, which is not process-based and instead creates particles supraglacially in a spatially- and temporally-regular manner, i.e. with seeding occurring in 20% of grid cells exclusive to the accumulation zone, and regularly every 300 yrs. This simpler scheme also produces less particles (~2.1 million at maximum) than the original seeding scheme. ii) The second sensitivity test uses the same ‘complex’ seeding as the original scheme (Fig. 2) but employs the parameter values of a different ensemble simulation (i.e. number 24) within the set of 8 Not-Ruled-Out-Yet simulations obtained by Leger et al. (2025). Whilst featuring different ensemble-varying parameter values (see Table S1 in Leger et al., 2025), simulation 24 produces Alps-wide model-data agreements in LGM ice extent and thickness that are indistinguishable from simulation 37 (used throughout this study). Input parameter differences (n=10) however generate changes in SMB, the basal sliding parameterization, ice rheology, and the magnitude of isostatic deflection. Importantly, simulation 24 uses a different bed topography than simulation 37, with no removal of valley-fill sediments.

In the first sensitivity test, which uses ‘simple’ seeding instead, model agreement with the locations of dated erratics presented above (section 3.4.2) decreases from 81-68% to 74-58%, with these two ranges representing whether we tolerate the small (<4 km) increase in ice extent mentioned above (section 3.4.2). Whilst not substantial, this decrease in model-data agreement is noticeable and suggests that a less process-based particle seeding scheme leads to a worse model-data fit on the provenance, glacial transport, and deposition histories of ice-contact deposits during the LGM. In the second sensitivity test, as the seeding scheme is unchanged from the original (see section 2.2), we can use provenance fractions (%) per hydrological basin (n=241) for each sink (see section 2.4) to quantify inter-simulation differences. Here, when using parameters from Leger et al. (2025)’s ensemble simulation 24 instead of 37, we find that particle provenance fractions per hydrological basin (e.g. percentages in Figs. 6, 8) remain identical in ~72% of cases, on average (median difference: 28.5%). When comparing particles’ provenance basins irrespective of fraction percentages, we find sink particles originate from the same basins in 88.5% of cases. Thus, running a simulation which yields a similar LGM model-data fit but uses different sensitive parameter values causes sink particles to originate from different basins in 11.5% of cases and provenance fractions to vary by 28.5% on average. These results show a non-negligible inter-simulation variability highlighting a noticeable sensitivity of particle trajectories and provenances to modelled ice dynamics and/or bed topography changes. However, this test also shows that the majority of particle trajectories, provenances, and glacial transport histories remain unchanged relative to the original simulation.

4 Discussion

4.1 Applications, limitations and future work

The computational gains of our novel GPU-based glacier modelling coupled with 3D Lagrangian particle tracking enabled us to produce an Alps-wide estimation of transient glacial sediment pathways during the last glaciation (40-18 ka). The results of this experiment are presented in the form of figure catalogues and trajectory shapefiles accessible via the Zenodo repository attached to this paper (link: https://doi.org/10.5281/zenodo.18374156). They provide the means to compare our spatially distributed modelling estimates against empirical evidence on, for instance, deposited LGM erratics and their lithologies/provenance, former ice-flow direction during the LGM, documented ice transfluences, and preserved post-retreat deposits and mapped moraines. We believe this first Alps-wide reconstruction of LGM glacial sediment transport will prove useful to glacial geologists, geomorphologists, sedimentologists, and industries studying ice-contact sediments related to the last glaciation of the European Alps. This new ability to conduct coupled glacier-particle modelling over continental and multi-millennial scales opens the door to new model-data comparisons which, in turn, can further improve the accuracy of future AIF models. Moreover, this study provides a novel, computationally efficient modelling workflow which opens the possibility to produce high-resolution estimates of the erosion, transport, and deposition dynamics of glacial sediments in numerous glaciated or formerly glaciated regions of the world.

4.2.1 Simplified glacial sediment transport dynamics

Although our model-data comparison of source-to-sink trajectories yields promising results with between 81% and 68% model fit with dated erratics' locations (section 3.4.2, Table S1), this study should be considered a first-order attempt yielding limitations and room for improvement. We describe below the main limitations of the assumptions made in this experiment, providing suggestions for improvement in future modelling work of similar nature. In this study, we assume passive particle glacial transport with no interaction with ice rheology and flow dynamics. In reality, supraglacial debris can influence glacier surface mass balance through insulation (e.g. Rowan et al., 2015) while basal ice sediments can alter basal friction and thus glacier sliding velocities (Hallet, 1981; Iverson et al., 2003). Our modelling also assumes all glacial sediments to move at the same velocity as the ice. Whilst this is a common modelling assumption (e.g. Rowan et al., 2015; Jouvet et al., 2017; Bernard et al., 2020; Margirier et al., 2025), the drag force in Stokes Law can cause resistance and lower velocities for clasts advected within highly viscous fluids (e.g. ice; Byers et al., 2012). Moreover, complex mechanisms of sediment storage occur (e.g. lodgement tills) at partially coupled ice-bed interfaces causing sediment advection speeds below ice velocity (Alley et al., 1997; Evans et al., 2006). On the contrary, gravitational and fluvio-glacial transport within glacier systems can generate sediment advection speeds greater than ice velocity (Walder and Fowler, 1994). Gravitational englacial transport also occurs when a glacier features numerous fractures in which debris can fall, a mechanism that is not yet modelled in glacier-wide simulations. Sediment transport by rivers (proglacial) and subglacial drainage, whilst not modelled in this study, can also complexify deposits' transport histories by moving large sediment volumes further down-river prior to glacier re-entrainment (Lane et al., 2017). In future work, modelling these complex mechanisms would require full coupling of both subglacial hydrology and sediment-transport modules to glacier-evolution models. Whilst such coupling has already been implemented in single-glacier modelling studies (e.g. Delaney et al., 2023), the added computational cost remains a challenge for large spatial and temporal (paleo) timescales, and the lack of observation data on subglacial and bed conditions leaves the numerous additional parameters of such schemes poorly constrained.

We assume all sediment to be fully preserved during glacial transport, and that variability in ice-contact deposit provenance is exclusively controlled by variations in seeding and glacial transport histories. However, clast erosion during glacial transport also plays an important role. Indeed, glacial sediments transported over greater distances are more likely to spend time at the ice-bed interface where they typically undergo abrasion, crushing, or truncation (Boulton, 1978). With increasing time and transport distance, this can generate rounding and comminution of coarse sediments (e.g. boulders, cobbles) into finer fractions (e.g. silts, sands and gravels) which can be mobilized by subglacial hydrology and evacuated downstream. Subsequently, the likelihood of finding sediments from a specific source in ice-contact deposits tends to decrease with increasing distance from that source (Humlum, 1985). In future modelling work, more realistic provenance fractions may thus be obtained through parameterizations that reduce particle preservation as glacial transport time and distances increase. For instance, previous work attempting to empirically quantify, through either laboratory (e.g. Hooke and Iverson, 1995) or field (e.g. Hubbard et al., 1996) investigations, the deformation-induced comminution of subglacial sediments by analysing their facies and properties (e.g. clast shape and size, fractal dimension), could help implement such model parameterizations.

4.2.2 Simplified erosion and particle-seeding dynamics

Our particle seeding scheme assumes that all bed surfaces are equally susceptible to subglacial erosion and production of supraglacial debris via gravitational mass wasting. This is a simplification as different lithologies yield different hardnesses and varying susceptibilities to abrasion, plucking, frost shattering, weathering, and other erosion mechanisms (Moosdorf et al., 2018). The subglacial erosion susceptibility of distinct outcrops is also often dependent on local tectonic pre-conditioning (e.g. degree of rock faulting and fracturing). The accuracy of future coupled glacier-particle modelling may thus be increased by adding an erodibility index parameter controlling the seeding likelihood based on rock hardness, faulting, temperature-driven rock-permafrost conditions, and resistance to erosion, constrained by present-day geological observations and/or reconstructed past erosion rates (Gallach et al., 2021). A number of studies have already produced global (e.g. Moosdorf et al., 2018) or more regional Alps-specific (e.g. (Kühni and Pfiffner, 2001) maps of erodibility indexes based on various geological attributes, which could thus be leveraged for improved model parameterization.

Soft beds under temperate glaciers can become saturated with meltwater, leading to reduced effective pressure, lower basal yield stresses, and faster sliding velocities (Iverson et al., 1995). While a meltwater feedback on sliding is included in our thermo-mechanically coupled glacier model setup (Leger et al., 2025), we consistently assume a positive correlation between sliding velocities and subglacial particle seeding through abrasion and plucking (Fig. 2). However, this may not always be the case as water saturation of soft beds and reduced effective pressure can instead shield bed material from abrasion/plucking reducing sediment mobilization or causing local soft bed deformation to instead dominate (Boulton, 1979).

4.2.3 Underestimated diversity of glacial sediment trajectories

Finally, while our GPU-based approach enables us to track an unprecedented number of particles in ice (~20.5 million) given our simulations' spatio-temporal scales, sediments are ubiquitous in real glaciers. Moreover, our modelling also does not include the re-mobilization by glaciers and glaciofluvial systems of pre-LGM sediment deposits over multiple glacial cycles. We thus likely still underestimate the diversity of pathways glacial sediments may follow within a glacier system as complex as the former AIF during Late-Quaternary glaciations. However, as shown with this work, GPU-computing enables to lower the computational cost of coupled glacier-particle modelling by several orders of magnitude. This should motivate new modelling studies of this nature to include the tracking of large particle numbers, thus helping to identify the particle numbers that more fully represent the ubiquitous nature of glacial sediments within icefield and ice-sheet systems.

Given the limitations summarized above, it is clear our modelling does not fully capture the complexity of glacial sediment sourcing and transport on multi-millennial, Alps-wide scales. Therefore, the diversity of 1) provenances and glacial transport pathways for a given ice-contact deposit, and 2) possible ice-contact deposit locations for a given source lithology, are likely underestimated by our 'sink-to-source' and 'source-to-sink' analyses (e.g. Figs. 6, 9). However, we believe that our simulations still capture the majority of former glacial sediment transport pathways, as evidenced by the relatively good model-data fit obtained (81-68%) when comparing modelled particle trajectories for a given lithology with data on LGM-dated erratic locations (section 3.4.2, Table S1).

4.2.4 Simplified mapping of terminal ice-contact deposits

As described above (section 2.4), our sink-to-source analysis uses a subjective set of 49 sink polygons (Fig. 3a) covering the space between maximum time-independent margins of the modelled AIF and the updated LGM empirical outline of Ehlers et al. (2011). Our sink polygons thus result from a consistent yet simplified Alps-wide separation of large regions containing the LGM margins of former AIF outlet glaciers. An obvious future improvement would be to produce similar sink-to-source analyses for more specific sites yielding detailed glacial geomorphological mapping of ice-contact deposits, or for a more detailed Alps-wide map of individual glacio-terminal landforms that remain preserved to this day. However, the latter would require producing a digital (e.g. GIS database), open-access, Alps-wide map of preserved glacial geomorphology with geochronological constraints and a consistent naming convention (e.g. Glasser & Jansson, 2008; Clark et al., 2018). To our knowledge, such a valuable product is not yet available for the European Alps.

4.2 Coupled glacier-particle modelling; wider implications and perspectives

4.2.1 New perspectives for paleo glacier model-data comparisons

After modelling the final retreat of the AIF from its LGM margins (24-18 ka), our particle advection scheme deposits static particles in deglaciated regions which form moraine-like shapes (e.g. Fig. 11, Figures S3-6). The resulting spatial densities and shapes of these particle deposits are controlled by; 1) the modelled ice-margin shape and location at a given time, 2) the modelled ice margin retreat rate and residence time during maximum glacier extent, still-stands, and/or smaller re-advances, and 3) the supply of ice-advected particles to the glacier margins at a given model location and time. To improve the accuracy of the model regarding these three mechanisms, one could compare the spatial patterns of modelled particle deposits against the preserved glacio-geomorphological record (Fig. 11, Figures S3-6). Although this is not within the scope of this study, we believe this work opens the possibility to design new post-processing tools to automatically quantify the agreement between modelled particle deposits (post deglaciation) and preserved landforms such as terminal and lateral moraines. This could represent a novel approach to paleo model-data comparison that may complement existing tools (e.g. Ely et al., 2019; Archer et al., 2023, Veness et al., 2025) designed to automatically score transient paleo simulations and quantitatively evaluate model sensitivities to - and the adequacy of - input parameterizations and climate forcings (Fig. 11). Such comparison may also help identify mechanisms controlling the spatial heterogeneity of preserved ice-contact deposits found across deglaciated forelands and valleys today (Ivy-Ochs et al., 2022).

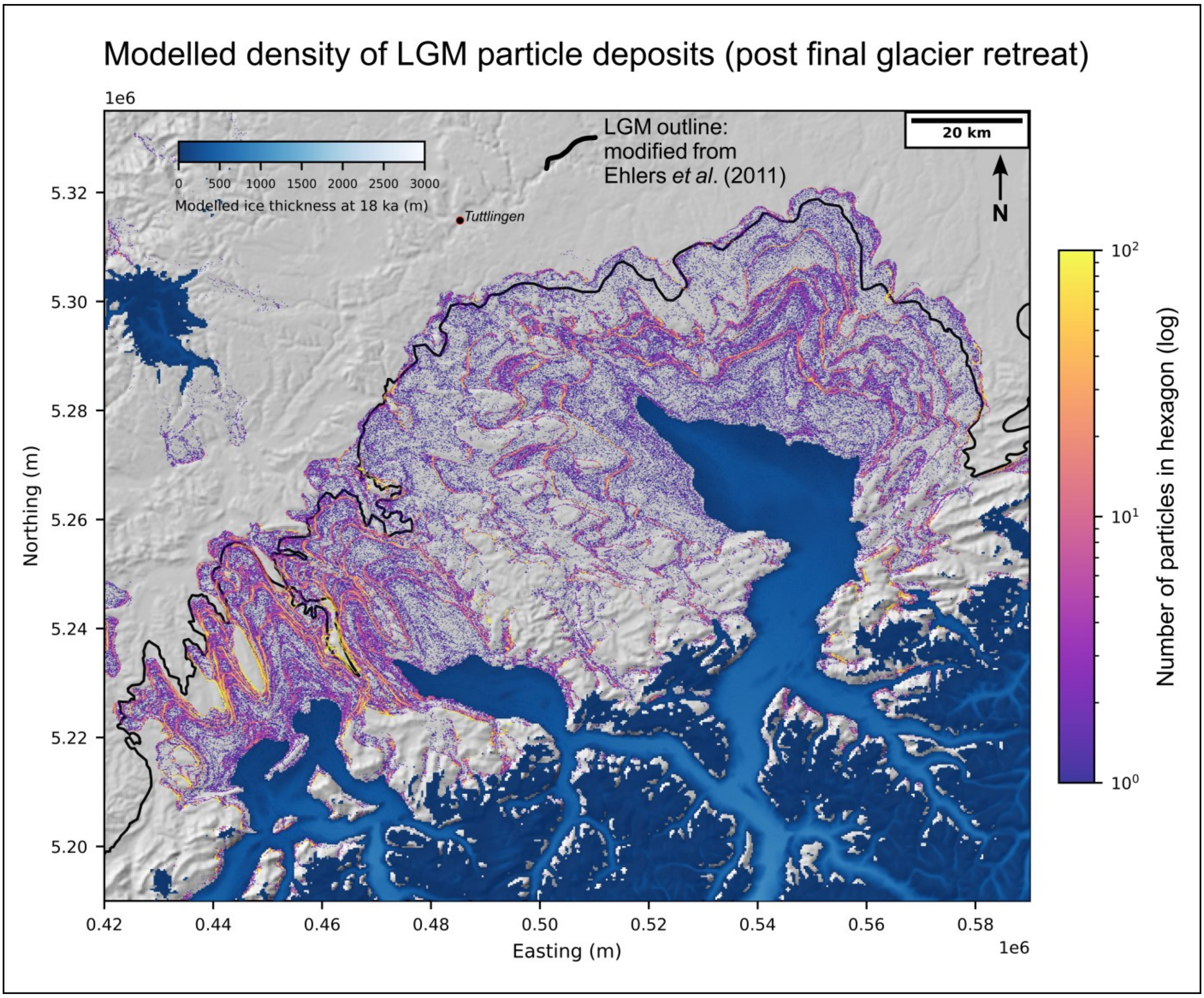

Figure 11. Map of modelled particle deposit densities located in modelled ice-free regions at 18 ka, the final timestep of our Alpine Ice Field (AIF) simulations of the Last Glacial Maximum (here 40-18 ka), and for the foreland region of the Rhein, Linth, and Reuss outlet glaciers. The AIF model output is displayed using modelled ice thickness at 18 ka. The particle deposit data shown here combines both datasets of particles seeded subglacially and supraglacially and is expressed as a spatial density map. Each colored dot is a small hexagon in which the total number of deposited particles is computed. Bright yellow colors indicate hexagons holding the highest concentrations of deposited particles. This model output clearly highlights periods of outlet glacier advances and/or margin stabilization during our AIF simulations through formation of moraine-shaped particle deposits. We argue the novel ability to produce such results over large spatio-temporal scales with our GPU-based Lagrangian particle tracking coupled to glacier evolution modelling may provide room for future model-data comparison exercises that quantify the fit between modelled particle deposits and the preserved glacio-geomorphological record (see Discussion section).

4.2.2 *A method to investigate complex internal ice-flow dynamics*

Lagrangian particle tracking coupled with glacier modelling essentially offers a mechanism to better visualize the time-transient 3D flow trajectories of simulated glacier motion (Figure S7). As a result, it can help to better understand contemporary and past internal glacier dynamics, including vertical ice motion, flow convergence and divergence, and the complex behaviours of merging glaciers. Provided that surge dynamics are realistically captured by the ice-flow model, particle tracking could also offer valuable insights into the transient flow complexity of surge-type glaciers and their associated sediment transport and deposition patterns. Such processes can be especially complicated in topographically constrained glacier complexes such as the former AIF. For instance, when two glaciers converge, their respective ice masses will become separated by a suture zone sometimes visible through formation of medial moraines (Small et al., 1979). Reconstructing the precise locations and lateral migrations of such suture zones in paleo glaciers, which reflect differences in driving stress and ice flux between two merging glaciers, can be crucial to explain: 1) the formation of specific subglacial landforms and their locations (e.g. lineations, drumlins and their orientations), 2) the lack or instead over-abundance of ice-contact deposits in specific locations, or 3) the puzzling provenances of specific sediments deposited at glacier margins. While such complex ice dynamics can be well-represented in glacier evolution models solving high-order ice-flow physics, particle tracking offers a means to easily visualize and quantify these processes (otherwise invisible) in model outputs. Our Mont Salève case study (section 3.3.3) is a good example for which understanding the location and migration of the suture zone separating the Rhône and Arve glaciers, easily visible with particles on Figure 8 (panel a), is key in understanding the modelled provenance and transport pathways of specific ice-contact deposits in this region (e.g. the Mont Salève erratics). Moreover, such coupled glacier-particle modelling can help target most appropriate field sites for future dating and/or provenance analyses of ice-contact deposits.

4.2.3 *Implications for research on glacial landscape evolution*

By combining our results with those of Leger et al. (2025), we demonstrate that GPU-parallelization can substantially decrease the computational cost of glacier evolution modelling coupled with Lagrangian particle tracking (Fig. 4). Besides helping to estimate glacial sediment transport trajectories over multi-millennial and continental spatio-temporal scales, we believe this new approach opens the door to a range of earth-surface modelling capabilities that may prove useful in addressing research questions in the fields of glaciology and mountain geomorphology. As an example, we believe there is potential for future model-data comparison studies to better characterize the role of glacial erosion on the relief development of mountain belts during Quaternary glaciations (e.g. Bernard et al., 2025), but also on more contemporary timescales (e.g. Delaney et al., 2023). Open questions remain, for instance, regarding the relative proportions of glacial erosion materials evacuated as glaciofluvial bed/suspended load versus frozen-on englacial debris, their role in controlling sediment export and deposition rates in the lowlands, and the spatio-temporal variability of these different processes under changing hydro-climatic conditions (Alley et al., 1998; Zhang et al., 2022; Fedotova & Magnani, 2024; Delaney et al., 2026). Large uncertainties remain also regarding subglacial mechanisms of sediment storage and resulting shielding of bedrock erosion, introducing sediment evacuation delays that are challenging to quantify, and which may bias current understandings of subglacial erosion’s correlation with basal glacier conditions including ice velocity and temperature (Herman et al., 2021; Delaney & Anderson, 2022). These challenging questions would benefit from new model-data comparison studies that bridge spatio-temporal gaps in empirical observations, thus making more holistic and fully coupled model frameworks involving particle tracking valuable tools for future investigations addressing these questions (Delaney et al., 2023).

To this day, one of the most advanced and efficient models coupling glacier-flow simulations with processes of fluvial and hillslope erosion, subglacial erosion, subglacial hydrology, and sediment transport over multi-millennial timescales, is the integrated second-order shallow ice approximation model (iSOSIA; Egholm et al., 2011). However, it remains computationally unfeasible to run such a CPU-based model over entire mountain ranges (e.g. the Alps), Quaternary-glaciation timescales (10^4-10^6 yr), and at the high spatial resolutions (<500 m) required to accurately resolve steep mountain topographies (Bernard et al., 2025). On the other hand, recent advances in GPU-optimized modelling and physics-informed machine learning have enabled to overcome such computational bottlenecks whilst in some cases respecting high-order 3D physics (e.g. Jouvet & Cordonnier, 2023; Cordonnier et al., 2023; Jain et al., 2024; Leger et al., 2025). The efficient GPU-parallelization of Lagrangian tracking will enable incorporating end-to-end advection of large particle numbers within fully coupled glacier-and-landscape evolution models. Therefore, it seems plausible that over the next few years, GPU-based modelling approaches permit high-resolution simulations whose outputs can be directly compared against empirical data on, for instance, Quaternary glacier incision rates and timing (e.g. Valla et al., 2011) or sediment export volumes and provenance data (e.g. Herman et al., 2015; Koppes et al., 2015; Overeem et al., 2017). Such model-data comparisons may shed light on the complex mechanisms influencing the dynamics of glacial erosion and its interaction with climate and topographic change over various spatio-temporal scales.

5. Conclusion

This study presents the first modelling reconstruction of sediment transport by glaciers across the entire European Alps during the Last Glacial Maximum (LGM). This is achieved using the GPU-accelerated Instructed Glacier Model (IGM) and by coupling 3D Lagrangian particle tracking with the high-resolution glacier simulations of Leger et al. (2025); an approach applied here for the first time at the scale of a continental icefield, with tens of millions of particles. This enables us to simulate complex, time-transient glacial sediment transport trajectories across the Alps over multi-millennial timescales (40-18 ka), and at an unprecedentedly high spatial resolution (300 m). Here, a key methodological innovation is the development of process-based particle seeding schemes for both subglacial and supraglacial sediment origins over large spatial scales, attempting to capture distinct erosion and debris entrainment dynamics. Our GPU-based approach significantly reduces the computational cost of Lagrangian tracking, making it feasible to track tens of millions of particles within glacier evolution models ran over continental domains, which represents a computational breakthrough for glacial sediment modelling.

Our two complementary sets of results, i.e. the sink-to-source (reconstructing ice-contact deposit provenance) and source-to-sink (mapping potential depositional locations) analyses, yield Alps-wide estimates of LGM glacial sediment routing, transport times, erosion timing, and cumulative ice-free exposure. The full results of these analyses are presented in two catalogues accessible via the Zenodo repository attached to this publication. We find particles of supraglacial origin are typically eroded earlier in time (i.e. are older), experience longer glacier residence times, and more cumulative ice-free exposure, with implications for interpreting cosmogenic nuclide inheritance signals in surface exposure dating for instance.

By presenting case studies such as the Mont Salève erratics transport histories, we also show how our modelling can address empirical hypotheses by reconstructing detailed particle trajectories consistent with known lithologies, which can in certain cases suggest revised paleo ice-flow interpretations. After comparing model results against empirical data, we find that sediment trajectories overlap with dated erratic boulders in 81-68% of cases, supporting the reliability of the approach and validating the use of process-based particle seeding schemes over simpler methods. Furthermore, our results enable us to precisely detect and map multiple LGM ice transfluences, including previously unreported overflow pathways, and estimate their occurrence durations, thus offering new perspectives on complex internal ice-flow and topographically uncoupled glacier dynamics across the Alps.

We believe our Alps-wide modelling of LGM glacial sediment transport and ice-flow dynamics provides a range of predictions that will prove useful to glacial geologists, geomorphologists, sedimentologists and industries studying ice-contact sediments related to Late-Quaternary glaciations in the European Alps.

Finally, IGM's computationally-efficient and GPU-based glacier-particle modelling framework opens new avenues for quantitative model-data comparisons using preserved glacial geomorphology and provides a powerful tool to study and better constrain paleo ice dynamics, sediment provenance, and Quaternary glacial landscape evolution.

Code and data availability.

The data that represent the main findings of this study: namely the 'sink-to-source', 'source-to-sink', 'ice-transfluence' data catalogues and their corresponding particle-trajectory polyline shapefiles are available from the following Zenodo open-access online repository: https://doi.org/10.5281/zenodo.18374156. This repository also features a series of videos displaying Alps-wide results from our Instructed Glacier Model (IGM) simulations including the visual rendering of particle advection and deposition for both subglacial and supraglacial seeding and zoomed in for 10 different regions of the Alps. These videos are also accessible via the IGM YouTube channel: https://www.youtube.com/@IGMGlacierModel/playlists. Finally, this repository also features codes, files and detailed instructions required to reproduce this study's specific IGM simulations using the correct IGM version (2.2.1.). Note that whilst the full modelled particle database produced in this study is too large to be stored online and shared (~1.22 TB), readers are encouraged to contact the corresponding author if wishing to compute and display particle trajectories for specific sinks or sources.

The IGM source code (Python programming language) which now includes the fully GPU-optimized particle-tracking module (in IGM versions ≥2.2.3) is open access and available from the GitHub repository at https://github.com/instructed-glacier-model/igm.git. IGM's documentation is available from its official website at https://igm-model.org/.

Supplement.

The supplement related to this article is available online at: ………..

Author contributions.

T.P.M.L., G.J., and M.B. conceived and designed the study with input ideas from S.K., A.V., A.H., F.H. and S.N. G.J. developed the original version of IGM, including the Lagrangian particle-tracking module in IGM, whose code was then modified and improved by B.F. within the context of this study to become fully GPU-optimised, with tests and compute-time diagnostics from T.P.M.L. T.P.M.L. designed and coded the particle seeding schemes and carried out the IGM simulations. T.P.M.L. created the post-processing coding workflow for particle trajectory extraction and mapping, with help from B.A. who optimized the Python code for efficient search of the large output particle database. T.P.M.L. compiled and generated the hydrological basin, ice-contact deposit, and surface lithology databases required for running the 'sink-to-source' and 'source-to-sink' analyses presented above. S.K. contributed to the extraction and mapping of certain surface lithologies. T.P.M.L. conducted the model-data comparison against erratic boulder data leveraging prior literature data mining and exposure-age recalculations from S.K. T.P.M.L. ran model sensitivity analyses, wrote the manuscript, and produced all figures and supplementary materials. All co-authors contributed to the discussions, interpretations and gave feedback on the final manuscript and figures.

Competing interests.

The contact author has declared that none of the authors have any competing interests.

Acknowledgements.

All IGM simulations were carried out on ‘Octopus’, a local computing cluster at the University of Lausanne, Faculty of GeoSciences and the Environnement (FGSE), managed by Dr. Ludovic Raess (University of Lausanne) whom we wish to thank for his work and support. We thank Prof. Jean-Luc Epard, Prof. Bernhard Salcher, Prof. Franz Neubauer, Dr. Jürgen M. Reitner and Dr. Jean-Daniel Champagnac for insightful discussions and for their precious help identifying alpine surface lithologies of particular relevance to this work. This work also benefited from discussions with Dr. Remy Veness, Dr. Julien Seguinot, Kejdi Lleshi, and Prof. Georgina King, whom we wish to thank. Finally, we wish to thank the two reviewers for their insightful comments and feedback which greatly improved the quality of the paper.

Financial support.

This research was funded by the Swiss National Science Foundation, through a grant (RECONCILE: project number: 213077) awarded to G.J, A.V., and S.N.

References

Aaron, J.: ORIN-3D – A new model for efficient simulation of landslide motion on a GPU using CUDA, Comput. Geotech., 153, 105078, https://doi.org/10.1016/j.compgeo.2022.105078, 2023.

Agassiz, L.: Études sur les glaciers, Aux frais de l'auteur. En commission chez Jent et Gassmann, libraires., Soleure, https://doi.org/https://doi.org/10.1017/CBO9781139235877, 1840.

Alley, R. B., Cuffey, K. M., Evenson, E. B., Strasser, J. C., Lawson, D. E., and Larson, G. J.: How glaciers entrain and transport basal sediment: Physical constraints, Quat. Sci. Rev., 16, 1017–1038, https://doi.org/10.1016/S0277-3791(97)00034-6, 1997.

Alley, R. B., Lawson, D. E., Evenson, E. B., Strasser, J. C., and Larson, G. J.: Glaciohydraulic supercooling: a freeze-on mechanism to create stratified, debris-rich basal ice: II. Theory, Journal of Glaciology, 44, 563–569, https://doi.org/10.3189/S0022143000002070, 1998.

Archer, R. E., Ely, J. C., Heaton, T. J., Butcher, F. E. G., Hughes, A. L. C., and Clark, C. D.: Assessing ice sheet models against the landform record: The Likelihood of Accordant Lineations Analysis (LALA) tool, Earth Surf. Process. Landf., 48, 2754–2771, https://doi.org/10.1002/esp.5658, 2023.

Aschwanden, A., Bueler, E., Khroulev, C., and Blatter, H.: An enthalpy formulation for glaciers and ice sheets, Journal of Glaciology, 58, 441–457, https://doi.org/10.3189/2012JoG11J088, 2012.

Benn, D. I., Bolch, T., Hands, K., Gulley, J., Luckman, A., Nicholson, L. I., Quincey, D., Thompson, S., Toumi, R., and Wiseman, S.: Response of debris-covered glaciers in the Mount Everest region to recent warming, and implications for outburst flood hazards, Earth. Sci. Rev., 114, 156–174, https://doi.org/10.1016/j.earscirev.2012.03.008, 2012.

Bernard, M., Steer, P., Gallagher, K., and Lundbek Egholm, D.: Modelling the effects of ice transport and sediment sources on the form of detrital thermochronological age probability distributions from glacial settings, Earth Surface Dynamics, 8, 931–953, https://doi.org/10.5194/esurf-8-931-2020, 2020.

Bernard, M., van der Beek, P. A., Pedersen, V. K., and Colleps, C.: Production and Preservation of Elevated Low-Relief Surfaces in Mountainous Landscapes by Pliocene-Quaternary Glaciations, AGU Advances, 6, https://doi.org/10.1029/2024AV001610, 2025.

Bichler, M. G., Reindl, M., Reitner, J. M., Drescher-Schneider, R., Wirsig, C., Christl, M., Hajdas, I., and Ivy-Ochs, S.: Landslide deposits as stratigraphical markers for a sequence-based glacial stratigraphy: a case study of a Younger Dryas system in the Eastern Alps, Boreas, 45, 537–551, https://doi.org/10.1111/bor.12173, 2016.

Bigi, G., Castellarin, A., Coli, M., Dal Piaz, G. V., Sartori, R., Scandone, P., and Vai, G.: Structural Model of Italy scale 1:500,000, sheet 1, Florence, 1990a.

Bigi, G., Castellarin, A., Coli, M., Dal Piaz, G. V., and Vai, G.: Structural Model of Italy scale 1:500,000, sheet 2, Florence, 1990b.

Blatter, H.: Velocity and stress fields in grounded glaciers: a simple algorithm for including deviatoric stress gradients, Journal of Glaciology, 41, 333–344, https://doi.org/10.3189/S002214300001621X, 1995.

Boulton, G. S.: Boulder shapes and grain-size distributions of debris as indicators of transport paths through a glacier and till genesis, Sedimentology, 25, 773–799, https://doi.org/10.1111/j.1365-3091.1978.tb00329.x, 1978.

Boulton, G. S.: Processes of Glacier Erosion on Different Substrata, Journal of Glaciology, 23, 15–38, https://doi.org/10.3189/S0022143000029713, 1979.

Boulton, G. S.: Theory of glacial erosion, transport and deposition as a consequence of subglacial sediment deformation, Journal of Glaciology, 42, 43–62, https://doi.org/10.3189/S0022143000030525, 1996.

Boxleitner, M., Ivy-Ochs, S., Egli, M., Brandova, D., Christl, M., and Maisch, M.: Lateglacial and Early Holocene glacier stages - New dating evidence from the Meiental in central Switzerland, Geomorphology, 340, 15–31, https://doi.org/10.1016/j.geomorph.2019.04.004, 2019.

Braakhekke, J., Ivy-Ochs, S., Monegato, G., Gianotti, F., Martin, S., Casale, S., and Christl, M.: Timing and flow pattern of the Orta Glacier (European Alps) during the Last Glacial Maximum, Boreas, 49, 315–332, https://doi.org/10.1111/bor.12427, 2020.

Bueler, E. and van Pelt, W.: Mass-conserving subglacial hydrology in the Parallel Ice Sheet Model version 0.6, Geosci. Model Dev., 8, 1613–1635, https://doi.org/10.5194/gmd-8-1613-2015, 2015.

Buoncristiani, J.-F. and Campy, M.: Quaternary Glaciations in the French Alps and Jura, in: Quaternary Glaciations - Extent and Chronology - a closer look, vol. 15, edited by: Ehlers, J., Gibbard, P. L., and Hughes, P. D., 117–126, https://doi.org/10.1016/B978-0-444-53447-7.00010-6, 2011.

Bussien Grosjean, D., Meisser, N., May-Leresche, S., Ulianov, A., and Vonlanthen, P.: The Morcles microgranite (Aiguilles Rouges, Swiss Alps): geochronological and geochemical evidences for a common origin with the Vallorcine intrusion, Swiss J. Geosci., 111, 35–49, https://doi.org/10.1007/s00015-017-0282-3, 2018.

Byers, J., Cohen, D., and Iverson, N. R.: Subglacial clast/bed contact forces, Journal of Glaciology, 58, 89–98, https://doi.org/10.3189/2012JoG11J126, 2012.

Calov, R. and Greve, R.: A semi-analytical solution for the positive degree-day model with stochastic temperature variations, Journal of Glaciology, 51, 173–175, https://doi.org/10.3189/172756505781829601, 2005.

Campy, M.: Palaeogeographical relationships between Alpine and Jura glaciers during the two last Pleistocene glaciations, Palaeogeogr. Palaeoclimatol. Palaeoecol., 93, 1–12, https://doi.org/10.1016/0031-0182(92)90180-D, 1992.

Capuzzo, N., Handler, R., Neubauer, F., and Wetzel, A.: Post-collisional rapid exhumation and erosion during continental sedimentation: the example of the late Variscan Salvan-Dorénaz basin (Western Alps), International Journal of Earth Sciences, 92, 364–379, https://doi.org/10.1007/s00531-003-0332-0, 2003.

Champel, B., van der Beek, P., Mugnier, J., and Leturmy, P.: Growth and lateral propagation of fault-related folds in the Siwaliks of western Nepal: Rates, mechanisms, and geomorphic signature, J. Geophys. Res. Solid Earth, 107, https://doi.org/10.1029/2001JB000578, 2002.

Clark, C. D., Ely, J. C., Greenwood, S. L., Hughes, A. L. C., Meehan, R., Barr, I. D., Bateman, M. D., Bradwell, T., Doole, J., Evans, D. J. A., Jordan, C. J., Monteys, X., Pellicer, X. M., and Sheehy, M.: BRITICE Glacial Map, version 2: a map and GIS database of glacial landforms of the last British–Irish Ice Sheet, Boreas, 47, 11-e8, https://doi.org/10.1111/bor.12273, 2018.

Clark, C. D., Ely, J. C., Hindmarsh, R. C. A., Bradley, S., Ignéczi, A., Fabel, D., Ó Cofaigh, C., Chiverrell, R. C., Scourse, J., Benetti, S., Bradwell, T., Evans, D. J. A., Roberts, D. H., Burke, M., Callard, S. L., Medialdea, A., Saher, M., Small, D., Smedley, R. K., Gasson, E., Gregoire, L., Gandy, N., Hughes, A. L. C., Ballantyne, C., Bateman, M. D., Bigg, G. R., Doole, J., Dove, D., Duller, G. A. T., Jenkins, G. T. H., Livingstone, S. L., McCarron, S., Moreton, S., Pollard, D., Praeg, D., Sejrup, H. P., Van Landeghem, K. J. J., and Wilson, P.: Growth and retreat of the last British–Irish Ice Sheet, 31 000 to 15 000 years ago: the BRITICE-CHRONO reconstruction, Boreas, 51, 699–758, https://doi.org/10.1111/bor.12594, 2022.

Cogez, A., Herman, F., Pelt, É., Reuschlé, T., Morvan, G., Darvill, C. M., Norton, K. P., Christl, M., Märki, L., and Chabaux, F.: U-Th and 10Be constraints on sediment recycling in proglacial settings, Lago Buenos Aires, Patagonia, Earth Surface Dynamics, 6, 121–140, https://doi.org/10.5194/esurf-6-121-2018, 2018.

Cook, S. J., Swift, D. A., Kirkbride, M. P., Knight, P. G., and Waller, R. I.: The empirical basis for modelling glacial erosion rates, Nat. Commun., 11, 1–7, https://doi.org/10.1038/s41467-020-14583-8, 2020.

Cordonnier, G., Jouvet, G., Peytavie, A., Braun, J., Cani, M.-P., Benes, B., Galin, E., Guérin, E., and Gain, J.: Forming Terrains by Glacial Erosion, ACM Trans. Graph., 42, 1–14, https://doi.org/10.1145/3592422, 2023.

Coutterand, S.: Étude géomophologique des flux glaciaires dans les Alpes nord-occidentales au Pléistocène récent. Du maximum de la dernière glaciation aux premières étapes de la déglaciation., PhD thesis, Université de Savoie, Le Bourget du Lac, 1–468 pp., 2010.

Coutterand, S.: Origines des blocs erratiques du Salève, Arch. Sci., 70, 51–56, 2018.

Cuffey, K. M. and Patterson, W. S. B.: The physics of glaciers, Academic Press, 1–704 pp., 2010.

Davies, B. J., Roberts, D. H., Bridgland, D. R., Ó Cofaigh, C., Riding, J. B., Demarchi, B., Penkman, K. E. H., and Pawley, S. M.: Timing and depositional environments of a Middle Pleistocene glaciation of northeast England: New evidence from Warren House Gill, County Durham, Quat. Sci. Rev., 44, 180–212, https://doi.org/10.1016/j.quascirev.2010.02.003, 2012.

Davies, B. J., Darvill, C. M., Lovell, H., Bendle, J. M., Dowdeswell, J. A., Fabel, D., García, J.-L., Geiger, A., Glasser, N. F., Gheorghiu, D. M., Harrison, S., Hein, A. S., Kaplan, M. R., Martin, J. R. V., Mendelova, M., Palmer, A., Pelto, M., Rodés, Á., Sagredo, E. A., Smedley, R. K., Smellie, J. L., and Thorndycraft, V. R.: The evolution of the Patagonian Ice Sheet from 35 ka to the present day (PATICE), Earth. Sci. Rev., 204, 103152, https://doi.org/10.1016/j.earscirev.2020.103152, 2020.

Delaney, I. and Anderson, L. S.: Debris Cover Limits Subglacial Erosion and Promotes Till Accumulation, Geophys. Res. Lett., 49, https://doi.org/10.1029/2022GL099049, 2022.

Delaney, I., Anderson, L., and Herman, F.: Modeling the spatially distributed nature of subglacial sediment transport and erosion, Earth Surface Dynamics, 11, 663–680, https://doi.org/10.5194/esurf-11-663-2023, 2023.

Delaney, I., Margirier, A., Gevers, M., Jenkin, M., Leger, T., Vergara, I., Seguinot, J., Jouvet, G., Alexander Aitken, A. R., Lane, S., Herman, F., and King, G. E.: Increased Glacier Melt Across Millennia to Hours Enhances Erosion and Sediment Export Processes, J. Geophys. Res. Earth Surf., 131, https://doi.org/10.1029/2025JF008614, 2026.

Dielforder, A. and Hetzel, R.: The deglaciation history of the Simplon region (southern Swiss Alps) constrained by 10Be exposure dating of ice-molded bedrock surfaces, Quat. Sci. Rev., 84, 26–38, https://doi.org/10.1016/j.quascirev.2013.11.008, 2014.

Duprat-Oualid, F., Rius, D., Bégeot, C., Magny, M., Millet, L., Wulf, S., and Appelt, O.: Vegetation response to abrupt climate changes in Western Europe from 45 to 14.7k cal a BP: the Bergsee lacustrine record (Black Forest, Germany), J. Quat. Sci., 32, 1008–1021, https://doi.org/10.1002/jqs.2972, 2017.

Egholm, D. L., Knudsen, M. F., Clark, C. D., and Lesemann, J. E.: Modeling the flow of glaciers in steep terrains: The integrated second-order shallow ice approximation (iSOSIA), J. Geophys. Res. Earth Surf., 116, https://doi.org/10.1029/2010JF001900, 2011.

Ehlers, J., Gibbard, P. L., and Hughes, P. D.: Developments in quaternary sciences: quaternary glaciations-extent and chronology: a closer look, 1st ed., edited by: Ehlers, J., Gibbard, P. L., and Hughes, P. D., Elsevier, Amsterdam, 2–1118 pp., 2011.

Ely, J. C., Clark, C. D., Small, D., and Hindmarsh, R. C. A.: ATAT 1.1, the Automated Timing Accordance Tool for comparing ice-sheet model output with geochronological data, Geosci. Model Dev., 12, 933–953, https://doi.org/10.5194/gmd-12-933-2019, 2019.

Enkelmann, E. and Ehlers, T. A.: Evaluation of detrital thermochronology for quantification of glacial catchment denudation and sediment mixing, Chem. Geol., 411, 299–309, https://doi.org/10.1016/j.chemgeo.2015.07.018, 2015.

Esmark, J.: Bidrag til vor Jordklodes Historie, Magazin for Naturvidenskaberne, 2, 28–49, 1824.

Evans, D. J. A. and Benn, D. I.: A Practical Guide to the Study of Glacial Sediments, Routledge, 2004.

Evans, D. J. A., Phillips, E. R., Hiemstra, J. F., and Auton, C. A.: Subglacial till: Formation, sedimentary characteristics and classification, Earth. Sci. Rev., 78, 115–176, https://doi.org/10.1016/j.earscirev.2006.04.001, 2006.

Federici, P. R., Ribolini, A., and Spagnolo, M.: Glacial history of the Maritime Alps from the Last Glacial Maximum to the Little Ice Age, Geological Society, London, Special Publications, 433, 137–159, https://doi.org/10.1144/SP433.9, 2017.

Fedotova, A. and Magnani, M. B.: Glacial Erosion Rates Since the Last Glacial Maximum for the Former Argentino Glacier and Present-Day Upsala Glacier, Patagonia, J. Geophys. Res. Earth Surf., 129, https://doi.org/10.1029/2024JF007960, 2024.

Fischer, L., Purves, R. S., Huggel, C., Noetzli, J., and Haeberli, W.: On the influence of topographic, geological and cryospheric factors on rock avalanches and rockfalls in high-mountain areas, Natural Hazards and Earth System Sciences, 12, 241–254, https://doi.org/10.5194/nhess-12-241-2012, 2012.

Fischer, U. H., Bebiolka, A., Brandefelt, J., Follin, S., Hirschorn, S., Jensen, M., Keller, S., Kennell, L., Näslund, J.-O., Normani, S., Selroos, J.-O., and Vidstrand, P.: Radioactive Waste Under Conditions of Future Ice Ages, in: Snow and Ice-Related Hazards, Risks, and Disasters, edited by: Shroder, J. F., Haeberli, W., and Whiteman, C., Elsevier, Boston, 345–393, https://doi.org/10.1016/B978-0-12-394849-6.00011-1, 2015.

Fischer, U. H., Bebiolka, A., Brandefelt, J., Cohen, D., Harper, J., Hirschorn, S., Jensen, M., Kennell, L., Liakka, J., Näslund, J.-O., Normani, S., Stück, H., and Weitkamp, A.: Radioactive waste under conditions of future ice ages, in: Snow and Ice-Related Hazards, Risks, and Disasters, edited by: Haeberli, W. and Whiteman, C., Elsevier, 323–375, https://doi.org/10.1016/B978-0-12-817129-5.00005-6, 2021.

Florineth, D. and Schlüchter, C.: Reconstructing the Last Glacial Maximum (LGM) ice surface geometry and flowlines in the Central Swiss Alps, Eclogae Geologicae Helvetiae, 91, https://doi.org/10.5169/seals-168431, 1998.

Gallach, X., Perrette, Y., Lafon, D., Chalmin, É., Deline, P., Ravanel, L., Carcaillet, J., and Wallet, T.: A new method for dating the surface exposure age of granite rock walls in the Mont Blanc massif by reflectance spectroscopy, Quat. Geochronol., 64, 101–156, https://doi.org/10.1016/j.quageo.2021.101156, 2021.

Geikie, J.: The Alps during the Glacial Period, Bulletin of the American Geographical Society, 42, 192, https://doi.org/10.2307/200422, 1910.

Geologische Bundesanstalt Österreich: Geodaten - Blatt 197 Kötschach (1:50.000), Tethys RDR, Geologische Bundesanstalt (GBA), Wien, https://doi.org/https://doi.org/10.24341/tethys.90, 2021a.

Geologische Bundesanstalt Österreich: Geodaten - Blatt 198 Weißbriach (1:50.000), Tethys RDR, Geologische Bundesanstalt (GBA), Wien, https://doi.org/https://doi.org/10.24341/tethys.88, 2021b.

Gianotti, F., Forno, M. G., Ivy-Ochs, S., and Kubik, P. W.: New chronological and stratigraphical data on the Ivrea amphitheatre (Piedmont, NW Italy), Quaternary International, 190, 123–135, https://doi.org/10.1016/j.quaint.2008.03.001, 2008.

Gianotti, F., Forno, M. G., Ajassa, R., Cámara, F., Costa, E., Ferrando, S., Giardino, M., Lucchesi, S., Motta, L., Motta, M., Perotti, L., and Rossetti, P.: The Ivrea Morainic Amphitheatre as a Well Preserved Record of the Quaternary Climate Variability (PROGEO-Piemonte Project, NW Italy), in: Engineering Geology for Society and Territory - Volume 8, edited by: Lollino Giorgio and Giordan, D. and M. C. and C. B. and Y. I. and M. C., Springer International Publishing, Cham, 235–238, https://doi.org/10.1007/978-3-319-09408-3_39, 2015.

Gibbons, A. B., Megeath, Joe. D., and Pierce, K. L.: Probability of moraine survival in a succession of glacial advances, Geology, 12, 327, https://doi.org/10.1130/0091-7613(1984)12<327:POMSIA>2.0.CO;2, 1984.

Glasser, N. and Jansson, K.: The Glacial map of southern South America, J. Maps, 4, 175–196, https://doi.org/10.4113/jom.2008.1020, 2008.

Graf, A., Akçar, N., Ivy-Ochs, S., Strasky, S., Kubik, P. W., Christl, M., Burkhard, M., Wieler, R., and Schlüchter, C.: Multiple advances of Alpine glaciers into the Jura Mountains in the Northwestern Switzerland, Swiss J. Geosci., 108, 225–238, https://doi.org/10.1007/s00015-015-0195-y, 2015.

Guillon, H., Mugnier, J., Buoncristiani, J., Carcaillet, J., Godon, C., Prud'homme, C., van der Beek, P., and Vassallo, R.: Improved discrimination of subglacial and periglacial erosion using 10Be concentration measurements in subglacial and supraglacial sediment load of the Bossons glacier (Mont Blanc massif, France), Earth Surf. Process. Landf., 40, 1202–1215, https://doi.org/10.1002/esp.3713, 2015.

Hallet, B.: Glacial Abrasion and Sliding: their Dependence on the Debris Concentration in Basal Ice, Ann. Glaciol., 2, 23–28, https://doi.org/10.3189/172756481794352487, 1981.

Herman, F., Beyssac, O., Brughelli, M., Lane, S. N., Leprince, S., Adatte, T., Lin, J. Y. Y., Avouac, J.-P., and Cox, S. C.: Erosion by an Alpine glacier, Science (1979)., 350, 193–195, https://doi.org/10.1126/science.aab2386, 2015.

Herman, F., De Doncker, F., Delaney, I., Prasicek, G., and Koppes, M.: The impact of glaciers on mountain erosion, Nat. Rev. Earth Environ., 2, 422–435, https://doi.org/10.1038/s43017-021-00165-9, 2021.

Heyman, J., Stroeven, A. P., Harbor, J. M., and Caffee, M. W.: Too young or too old: Evaluating cosmogenic exposure dating based on an analysis of compiled boulder exposure ages, Earth Planet. Sci. Lett., 302, 71–80, https://doi.org/10.1016/j.epsl.2010.11.040, 2011.

Hippe, K., Ivy-Ochs, S., Kober, F., Zasadni, J., Wieler, R., Wacker, L., Kubik, P. W., and Schlüchter, C.: Chronology of Lateglacial ice flow reorganization and deglaciation in the Gotthard Pass area, Central Swiss Alps, based on cosmogenic 10Be and in situ 14C, Quat. Geochronol., 19, 14–26, https://doi.org/10.1016/j.quageo.2013.03.003, 2014.

Hooke, R. LeB. and Iverson, N. R.: Grain-size distribution in deforming subglacial tills: Role of grain fracture, Geology, 23, 57, https://doi.org/10.1130/0091-7613(1995)023<0057:GSDIDS>2.3.CO;2, 1995.

Hubbard, B., Sharp, M., and Lawson, W. J.: On the sedimentological character of Alpine basal ice facies, Ann. Glaciol., 22, 187–193, https://doi.org/10.3189/1996AoG22-1-187-193, 1996.

Hughes, A. L. C., Clark, C. D., and Jordan, C. J.: Subglacial bedforms of the last British Ice sheet, J. Maps, 6, 543–563, https://doi.org/10.4113/jom.2010.1111, 2010.

Humlum, O.: Changes in Texture and Fabric of Particles in Glacial Traction with Distance from Source, Mỳrdalsjökull, Iceland, Journal of Glaciology, 31, 150–156, https://doi.org/10.3189/S0022143000006390, 1985.

Humphrey, N. F. and Raymond, C. F.: Hydrology, erosion and sediment production in a surging glacier: Variegated Glacier, Alaska, 1982–83, Journal of Glaciology, 40, 539–552, https://doi.org/10.3189/S0022143000012429, 1994.

van Husen, D.: LGM and late-glacial fluctuations in the Eastern Alps, Quaternary International, 38–39, 109–118, https://doi.org/10.1016/S1040-6182(96)00017-1, 1997.

Iverson, N. R., Hanson, B., Hooke, R. LeB., and Jansson, P.: Flow Mechanism of Glaciers on Soft Beds, Science (1979)., 267, 80–81, https://doi.org/10.1126/science.267.5194.80, 1995.

Iverson, N. R., Cohen, D., Hooyer, T. S., Fischer, U. H., Jackson, M., Moore, P. L., Lappegard, G., and Kohler, J.: Effects of Basal Debris on Glacier Flow, Science (1979)., 301, 81–84, https://doi.org/10.1126/science.1083086, 2003.

Ivy-Ochs, S.: Glacier variations in the European Alps at the end of the last glaciation, Cuadernos de Investigación Geográfica, 41, 295–315, https://doi.org/10.18172/cig.2750, 2015.

Ivy-Ochs, S., Schäfer, J., Kubik, P. W., Synal, H. A., and Schlüchter, C.: Timing of deglaciation on the northern Alpine foreland (Switzerland), Eclogae Geologicae Helvetiae, 97, 47–55, https://doi.org/10.1007/s00015-004-1110-0, 2004.

Ivy-Ochs, S., Lucchesi, S., Baggio, P., Fioraso, G., Gianotti, F., Monegato, G., Graf, A. A., Akçar, N., Christl, M., Carraro, F., Forno, M. G., and Schlüchter, C.: New geomorphological and chronological constraints for glacial deposits in the Rivoli-Avigliana end-moraine system and the lower Susa Valley (Western Alps, NW Italy), J. Quat. Sci., 33, 550–562, https://doi.org/10.1002/jqs.3034, 2018.

Ivy-Ochs, S., Monegato, G., and Reitner, J. M.: The Alps: glacial landforms from the Last Glacial Maximum, in: European Glacial Landscapes, edited by: Palacios, D., Hughes, P. D., García-Ruiz, J. M., and Andrés, N., Elsevier, 449–460, https://doi.org/10.1016/B978-0-12-823498-3.00030-3, 2022.

Jain, A., Kerbl, B., Gain, J., Finley, B., and Cordonnier, G.: FastFlow: GPU Acceleration of Flow and Depression Routing for Landscape Simulation, Computer Graphics Forum, 43, https://doi.org/10.1111/cgf.15243, 2024.

Jouvet, G. and Cordonnier, G.: Ice-flow model emulator based on physics-informed deep learning, Journal of Glaciology, 1–15, https://doi.org/10.1017/jog.2023.73, 2023.

Jouvet, G., Seguinot, J., Ivy-ochs, S., and Funk, M.: Modelling the diversion of erratic boulders by the Valais Glacier during the last glacial maximum, Journal of Glaciology, 63, 487–498, https://doi.org/10.1017/jog.2017.7, 2017.

Jouvet, G., Cordonnier, G., Kim, B., Lüthi, M., Vieli, A., and Aschwanden, A.: Deep learning speeds up ice flow modelling by several orders of magnitude, Journal of Glaciology, 68, 651–664, https://doi.org/10.1017/jog.2021.120, 2022.

Jouvet, G., Cohen, D., Russo, E., Buzan, J., Raible, C. C., Haeberli, W., Kamleitner, S., Ivy-Ochs, S., Imhof, M. A., Becker, J. K., Landgraf, A., and Fischer, U. H.: Coupled climate-glacier modelling of the last glaciation in the Alps, Journal of Glaciology, 1–15, https://doi.org/10.1017/jog.2023.74, 2023.

Jouvet, G., Cook, S., Cordonnier, G., Finley, B., Henz, A., Herrmann, O., Maussion, F., Mey, J., Scherler, D., and Welty, E.: Concepts and capabilities of the Instructed Glacier Model, https://doi.org/10.31223/X5T99C, 7 April 2024.

Kamleitner, S., Ivy-Ochs, S., Monegato, G., Gianotti, F., Akçar, N., Vockenhuber, C., Christl, M., and Synal, H.-A.: The Ticino-Toce glacier system (Swiss-Italian Alps) in the framework of the Alpine Last Glacial Maximum, Quat. Sci. Rev., 279, 107400, https://doi.org/10.1016/j.quascirev.2022.107400, 2022.

Kamleitner, S., Ivy-Ochs, S., Manatschal, L., Akçar, N., Christl, M., Vockenhuber, C., Hajdas, I., and Synal, H.-A.: Last Glacial Maximum glacier fluctuations on the northern Alpine foreland: Geomorphological and chronological reconstructions from the Rhine and Reuss glacier systems, Geomorphology, 423, 108548, https://doi.org/10.1016/j.geomorph.2022.108548, 2023.

Kamleitner, S., Leger, T. P. M., Ivy-Ochs, S., Nussbaumer, S. U., Vieli, A., and Jouvet, G.: AlpIce - Towards an Alps-wide database of empirical geo(morpho)logical and geochronological data constraining Last Glacial Maximum to Holocene glacier fluctuations, in: EGU General Assembly 2024, https://doi.org/10.5194/egusphere-egu24-9282, 2024a.

Kamleitner, S., Ivy-Ochs, S., Salcher, B., and Reitner, J. M.: Reconstructing basal ice flow patterns of the Last Glacial Maximum Rhine glacier (northern Alpine foreland) based on streamlined subglacial landforms, Earth Surf. Process. Landf., 49, 746–769, https://doi.org/10.1002/esp.5733, 2024b.

Keller, O. and Krayss, E.: Mittel- und spätpleistozäne Stratigraphie und Morphogenese in Schlüsselregionen der Nordschweiz, E&G Quaternary Science Journal, 59, 88–119, https://doi.org/10.3285/eg.59.1-2.08, 2011.

Kelly, M. A., Buoncristiani, J.-F., and Schlüchter, C.: A reconstruction of the last glacial maximum (LGM) ice-surface geometry in the western Swiss Alps and contiguous Alpine regions in Italy and France, Eclogae Geologicae Helvetiae, 97, 57–75, https://doi.org/10.1007/s00015-004-1109-6, 2004.

Koppes, M., Hallet, B., Rignot, E., Mouginot, J., Wellner, J. S., and Boldt, K.: Observed latitudinal variations in erosion as a function of glacier dynamics, Nature, 526, 100–103, https://doi.org/10.1038/nature15385, 2015.

Kühni, A. and Pfiffner, O. A.: The relief of the Swiss Alps and adjacent areas and its relation to lithology and structure: topographic analysis from a 250-m DEM, Geomorphology, 41, 285–307, https://doi.org/10.1016/S0169-555X(01)00060-5, 2001.

Lane, S. N., Bakker, M., Gabbud, C., Micheletti, N., and Saugy, J.-N.: Sediment export, transient landscape response and catchment-scale connectivity following rapid climate warming and Alpine glacier recession, Geomorphology, 277, 210–227, https://doi.org/10.1016/j.geomorph.2016.02.015, 2017.

Leger, T. P. M., Jouvet, G., Kamleitner, S., Mey, J., Herman, F., Finley, B. D., Ivy-Ochs, S., Vieli, A., Henz, A., and Nussbaumer, S. U.: A data-consistent model of the last glaciation in the Alps achieved with physics-driven AI, Nat. Commun., 16, 848, https://doi.org/10.1038/s41467-025-56168-3, 2025.

Lehner, B. and Grill, G.: Global river hydrography and network routing: baseline data and new approaches to study the world's large river systems, Hydrol. Process., 27, 2171–2186, https://doi.org/10.1002/hyp.9740, 2013.

Letsch, D., Winkler, W., von Quadt, A., and Gallhofer, D.: The volcano-sedimentary evolution of a post-Variscan intramontane basin in the Swiss Alps (Glarus Verrucano) as revealed by zircon U–Pb age dating and Hf isotope geochemistry, International Journal of Earth Sciences, 104, 123–145, https://doi.org/10.1007/s00531-014-1055-0, 2015.

Linton, D. L.: Watershed Breaching by Ice in Scotland, Transactions and Papers (Institute of British Geographers), 1, https://doi.org/10.2307/621028, 1949.

Luetscher, M., Boch, R., Sodemann, H., Spötl, C., Cheng, H., Edwards, R. L., Frisia, S., Hof, F., and Müller, W.: North Atlantic storm track changes during the Last Glacial Maximum recorded by Alpine speleothems, Nat. Commun., 6, 6344, https://doi.org/10.1038/ncomms7344, 2015.

Lyell, C.: On the geological evidence of the former existence of glaciers in Forfarshire, Proceedings of the Geological Society of London, 3, 337–345, 1840.

Manzotti, P.: Petro-structural map of the Dent Blanche tectonic system between Valpelline and Valtournenche valleys, Western Italian Alps, J. Maps, 7, 340–352, https://doi.org/10.4113/jom.2011.1179, 2011.

Margirier, A., Brondex, J., Rowan, A. V., Schmidt, C., Pedersen, V. K., Lehmann, B., Anderson, L. S., Veness, R., Watson, C. S., Swift, D., and King, G. E.: Tracking Sediment Transport Through Miage Glacier, Italy, Using a Lagrangian Approach With Luminescence Rock Surface Burial Dating of Englacial Clasts, J. Geophys. Res. Earth Surf., 130, https://doi.org/10.1029/2024JF007773, 2025.

Mathes, N., Luetscher, M., Ivy-Ochs, S., Dieleman, C., Christl, M., Vockenhuber, C., and Akçar, N.: An extensive MIS 12 Alpine glaciation in the Jura Mountains: insights from cave sediments and burial dating, Quat. Sci. Rev., 376, 109818, https://doi.org/10.1016/j.quascirev.2026.109818, 2026.

Matthews, J. A., Shakesby, R. A., and Fabel, D.: Very low inheritance in cosmogenic surface exposure ages of glacial deposits: A field experiment from two Norwegian glacier forelands, Holocene, 27, 1406–1414, https://doi.org/10.1177/0959683616687387, 2017.

Mey, J., Scherler, D., Wickert, A. D., Egholm, D. L., Tesauro, M., Schildgen, T. F., and Strecker, M. R.: Glacial isostatic uplift of the European Alps, Nat. Commun., 7, 13382, https://doi.org/10.1038/ncomms13382, 2016.

Mohammadi, M., McMackin, C., and Egli, M.: Source identification of morainic materials in soils of the Three Lakes region (Switzerland) using the fingerprinting technique, Catena (Amst)., 234, 107619, https://doi.org/10.1016/j.catena.2023.107619, 2024.

Monegato, G., Scardia, G., Hajdas, I., Rizzini, F., and Piccin, A.: The Alpine LGM in the boreal ice-sheets game, Sci. Rep., 7, 2078, https://doi.org/10.1038/s41598-017-02148-7, 2017.

Monegato, G., Kamleitner, S., Gianotti, F., Martin, S., Scapozza, C., and Ivy-Ochs, S.: The Ticino-Toce Ice Conveyor Belts During The Last Glacial Maximum, Alpine and Mediterranean Quaternary, 35, 119–134, https://doi.org/https://doi.org/10.26382/AMQ.2022.07, 2022.

Moosdorf, N., Cohen, S., and von Hagke, C.: A global erodibility index to represent sediment production potential of different rock types, Applied Geography, 101, 36–44, https://doi.org/10.1016/j.apgeog.2018.10.010, 2018.

Overeem, I., Hudson, B. D., Syvitski, J. P. M., Mikkelsen, A. B., Hasholt, B., van den Broeke, M. R., Noël, B. P. Y., and Morlighem, M.: Substantial export of suspended sediment to the global oceans from glacial erosion in Greenland, Nat. Geosci., 10, 859–863, https://doi.org/10.1038/ngeo3046, 2017.

Penck, A. and Brückner, E.: Die Alpen im Eiszeitalter, Tauchnitz, 1909.

Preusser, F., Reitner, J. M., and Schlüchter, C.: Distribution, geometry, age and origin of overdeepened valleys and basins in the Alps and their foreland, Swiss J. Geosci., 103, 407–426, https://doi.org/10.1007/s00015-010-0044-y, 2010.

Preusser, F., Graf, H. R., Keller, O., Krayss, E., and Schlüchter, C.: Quaternary glaciation history of northern Switzerland, E&G Quaternary Science Journal, 60, 282–305, https://doi.org/10.3285/eg.60.2-3.06, 2011.

Prud'homme, C., Vassallo, R., Crouzet, C., Carcaillet, J., Mugnier, J., and Cortés-Aranda, J.: Paired 10Be sampling of polished bedrock and erratic boulders to improve dating of glacial landforms: an example from the Western Alps, Earth Surf. Process. Landf., 45, 1168–1180, https://doi.org/10.1002/esp.4790, 2020.

Ravazzi, C., Badino, F., Marsetti, D., Patera, G., and Reimer, P. J.: Glacial to paraglacial history and forest recovery in the Oglio glacier system (Italian Alps) between 26 and 15 ka cal BP, Quat. Sci. Rev., 58, 146–161, https://doi.org/10.1016/j.quascirev.2012.10.017, 2012.

Reber, R., Akçar, N., Ivy-Ochs, S., Tikhomirov, D., Burkhalter, R., Zahno, C., Lüthold, A., Kubik, P. W., Vockenhuber, C., and Schlüchter, C.: Timing of retreat of the Reuss Glacier (Switzerland) at the end of the Last Glacial Maximum, Swiss J. Geosci., 107, 293–307, https://doi.org/10.1007/s00015-014-0169-5, 2014.

Reitner, J. M.: Glacial dynamics at the beginning of Termination I in the Eastern Alps and their stratigraphic implications, Quaternary International, 164–165, 64–84, https://doi.org/10.1016/j.quaint.2006.12.016, 2007.

Reitner, J. M., Gruber, W., Römer, A., and Morawetz, R.: Alpine overdeepenings and paleo-ice flow changes: an integrated geophysical-sedimentological case study from Tyrol (Austria), Swiss J. Geosci., 103, 385–405, https://doi.org/10.1007/s00015-010-0046-9, 2010.

Reynard, E.: Protecting stones: conservation of erratic blocks in Switzerland, in: Dimension stone, Taylor and Francis, London, 3–7, 2004.

Ribolini, A., Spagnolo, M., Cyr, A. J., and Federici, P. R.: Last Glacial Maximum and early deglaciation in the Stura Valley, southwestern European Alps, Quat. Sci. Rev., 295, 107770, https://doi.org/10.1016/j.quascirev.2022.107770, 2022.

Roattino, T., Crouzet, C., Vassallo, R., Buoncristiani, J. F., Carcaillet, J., Gribenski, N., and Valla, P. G.: Paleogeographical reconstruction of the western French Alps foreland during the last glacial maximum using cosmogenic exposure dating, Quaternary Research (United States), 111, 68–83, https://doi.org/10.1017/qua.2022.25, 2023.

Rowan, A. V., Egholm, D. L., Quincey, D. J., and Glasser, N. F.: Modelling the feedbacks between mass balance, ice flow and debris transport to predict the response to climate change of debris-covered glaciers in the Himalaya, Earth Planet. Sci. Lett., 430, 427–438, https://doi.org/10.1016/j.epsl.2015.09.004, 2015.

Russo, E., Buzan, J., Lienert, S., Jouvet, G., Velasquez Alvarez, P., Davis, B., Ludwig, P., Joos, F., and Raible, C. C.: High-resolution LGM climate of Europe and the Alpine region using the regional climate model WRF, Climate of the Past, 20, 449–465, https://doi.org/10.5194/cp-20-449-2024, 2024.

Rybak, O. and Huybrechts, P.: A comparison of Eulerian and Lagrangian methods for dating in numerical ice-sheet models, Ann. Glaciol., 37, 150–158, https://doi.org/10.3189/172756403781815393, 2003.

Scherler, D. and Egholm, D. L.: Production and Transport of Supraglacial Debris: Insights From Cosmogenic 10Be and Numerical Modeling, Chhota Shigri Glacier, Indian Himalaya, J. Geophys. Res. Earth Surf., 125, https://doi.org/10.1029/2020JF005586, 2020.

Schoof, C. and Hewitt, I.: Ice-Sheet Dynamics, Annu. Rev. Fluid Mech., 45, 217–239, https://doi.org/10.1146/annurev-fluid-011212-140632, 2013.

Seguinot, J. and Delaney, I.: Last-glacial-cycle glacier erosion potential in the Alps, Earth Surface Dynamics, 9, 923–935, https://doi.org/10.5194/esurf-9-923-2021, 2021.

Seguinot, J., Ivy-Ochs, S., Jouvet, G., Huss, M., Funk, M., and Preusser, F.: Modelling last glacial cycle ice dynamics in the Alps, Cryosphere, 12, 3265–3285, https://doi.org/10.5194/tc-12-3265-2018, 2018.

Small, R. J., Clark, M. J., and Cawse, T. J. P.: The Formation of Medial Moraines on Alpine Glaciers, Journal of Glaciology, 22, 43–52, https://doi.org/10.3189/S0022143000014040, 1979.

Sugden, David. E. and John, Brian. S.: Glaciers and Landscape: A Geomorphological Approach, 1st ed., Edward Arnold, London, 1–376 pp., 1976.

Tadono, T., Ishida, H., Oda, F., Naito, S., Minakawa, K., and Iwamoto, H.: Precise Global DEM Generation by ALOS PRISM, ISPRS Annals of the Photogrammetry, Remote Sensing and Spatial Information Sciences, II–4, 71–76, https://doi.org/10.5194/isprsannals-II-4-71-2014, 2014.

Valla, P. G., Shuster, D. L., and van der Beek, P. A.: Significant increase in relief of the European Alps during mid-Pleistocene glaciations, Nat. Geosci., 4, 688–692, https://doi.org/10.1038/ngeo1242, 2011.

Veness, R. L., Clark, C. D., Ely, J. C., Knight, J. L., Igneczi, A., and Bradley, S. L.: Modelling erratic dispersal accounting for shifting ice flow geometries: A new method and explanations of erratic dispersal of the British–Irish Ice Sheet, J. Quat. Sci., https://doi.org/10.1002/jqs.3720, 2025.

Venetz, I.: Sur l'ancienne extension des glaciers et sur leur retraite dans leur limites actuelles, in: Actes de la Société Helvétique des Sciences Naturelles. Quinzieme Réunion Annuelle à l'Hospice du Grand-Saint-Bernard, 21–22, 1830.

Walder, J. S. and Fowler, A.: Channelized subglacial drainage over a deformable bed, Journal of Glaciology, 40, 3–15, https://doi.org/10.3189/S0022143000003750, 1994.

Wang, B., Wald, I., Morrical, N., Usher, W., Mu, L., Thompson, K., and Hughes, R.: An GPU-accelerated particle tracking method for Eulerian–Lagrangian simulations using hardware ray tracing cores, Comput. Phys. Commun., 271, 108221, https://doi.org/10.1016/j.cpc.2021.108221, 2022.

Wickert, A. D.: Open-source modular solutions for flexural isostasy: gFlex v1.0, Geoscientific Model Development Discussions, 8, 4245–4292, https://doi.org/10.5194/gmdd-8-4245-2015, 2015.

Wüthrich, L., Morabito, E. G., Zech, J., Trauerstein, M., Veit, H., Gnägi, C., Merchel, S., Scharf, A., Rugel, G., Christl, M., and Zech, R.: 10Be surface exposure dating of the last deglaciation in the Aare Valley, Switzerland, Swiss J. Geosci., 111, 295–303, https://doi.org/10.1007/s00015-018-0298-3, 2018.

Zhang, T., Li, D., East, A. E., Walling, D. E., Lane, S., Overeem, I., Beylich, A. A., Koppes, M., and Lu, X.: Warming-driven erosion and sediment transport in cold regions, Nat. Rev. Earth Environ., 3, 832–851, https://doi.org/10.1038/s43017-022-00362-0, 2022.